

**RESISTIVE WALL AND ERROR FIELD
STUDIES USING THE EXTENDED MHD
CODE NIMROD**

By

Andrea L Becerra

A THESIS SUBMITTED IN PARTIAL FULFILLMENT OF THE
REQUIREMENTS FOR THE DEGREE OF

MASTER OF SCIENCE
(ENGINEERING PHYSICS)

at the

UNIVERSITY OF WISCONSIN – MADISON

2016

© Copyright by Andrea L Becerra 2016

All Rights Reserved

Abstract

The implementation of a resistive wall boundary condition has made possible the study of resistive wall modes (RWMs) in a variety of geometries using the extended MHD code NIMROD. While RWMs grow relatively slowly, they can lead to disruptions, and the wall itself can play a more complicated role in the interaction between plasma rotation and resonant error fields. A boundary condition specific to a periodic cylinder was developed and benchmarked against theoretical results for an analytically simple current step-function equilibrium. The boundary condition mechanism was leveraged to introduce a resonant error field allowing the nonlinear error-field-driven mode-locking process to be simulated in a periodic cylinder using NIMROD. A more general resistive wall boundary condition was developed which can work for both periodic cylinder and toroidal geometries. While the numerical convergence properties using this boundary condition were not optimal, the agreement with theory and prior simulation was good for the periodic cylinder case. This added NIMROD functionality was used with equilibrium reconstructions of the spherical torus NSTX from shots in which the normalized beta was scanned across the critical value for RWM stability. The magnitude of the RWM growth rate (or absence of a RWM) in the NIMROD results was used to estimate the critical normalized beta. This estimate was consistent with the critical value calculated by the stability code DCON. These promising results suggest that this boundary condition can be used to study more complicated nonlinear RWM physics in NIMROD.

Contents

Abstract	i
1 Introduction and Motivation	1
1.1 Critical Stability of Tokamaks	1
1.2 Resistive Wall and Associated Modes	1
1.3 Advantages and Necessity of Simulation	2
2 Background and Theory	4
2.1 Review of magnetohydrodynamics in tokamaks	4
2.1.1 Magnetohydrodynamic equations	4
2.1.2 Tokamak equilibria	5
2.2 Kink and resistive wall instabilities	9
2.2.1 Theory of kink instabilities	9
2.2.2 Theory of resistive wall instabilities	10
2.2.3 The vertical displacement event: a particularly nasty case of the RWM	10
2.2.4 Advancements in the understanding of RWM stability	11
2.3 Magnetic error fields or perturbations	13
2.3.1 Review of basic island and tearing mode physics	14
2.3.2 Theory of error field driven islands	16
2.3.3 Torque balance and mode-locking theory	18
2.3.4 The effects of error fields in experiment	22
2.4 Numerical implementations of a resistive wall and error fields	24
2.4.1 Codes for studying XK stability	24

2.4.2	The MARS code	24
2.4.3	The M3D and M3D-C1 codes	25
2.4.4	The AEGIS code	26
2.4.5	The coupled JOREK and STARWALL codes	26
2.4.6	Codes with external magnetic perturbations but no resistive wall . .	27
2.5	Overview of the NIMROD code	27
2.5.1	Equilibria for NIMROD	29
2.5.2	Spectral elements and Fourier representation of quantities	30
3	Resistive wall boundary condition for a periodic cylinder	32
3.1	Implementation in NIMROD	32
3.2	Top-hat current profile test case	35
3.3	Verification of NIMROD resistive wall boundary condition for a periodic cylinder	41
4	External error fields in a periodic cylinder	46
4.1	Implementation in NIMROD	46
4.2	Equilibrium for testing error-field driven islands in NIMROD	48
4.3	Linear simulation results from error field studies	50
4.4	Nonlinear simulation results from error field studies	53
5	General resistive wall boundary condition	57
5.1	Implementation in NIMROD	57
5.1.1	Natural boundary condition on the electric field	57
5.1.2	Dirichlet boundary condition on the normal magnetic field	58
5.1.3	Interpolation with GRIN	59
5.2	Resistive wall boundary condition verification	61

5.2.1	Verification in a periodic cylinder	61
5.2.2	Verification in a large-aspect-ratio torus	62
5.3	Spatial convergence studies	63
5.3.1	Convergence for a large aspect ratio torus	63
5.3.2	Convergence for a periodic cylinder	65
6	Simulating the RWM in NSTX	71
6.1	Modeling NSTX with NIMROD	72
6.2	Resistive wall parameter scan	74
6.3	Identifying the critical β_N for RWM stability	75
7	Conclusions	81
A	Derivation of Vacuum Response Matrix for Periodic Cylinder	83
A.1	Method 1	83
A.2	Method 2	87
B	General Normal Magnetic Field Boundary Condition	90
	References	93

Chapter 1

Introduction and Motivation

1.1 Critical Stability of Tokamaks

In order to progress towards energy production using magnetic confinement fusion, one major goal is to produce a stable, high-pressure plasma. The primary parameter used to characterize this is $\beta = 2\mu_0\langle p\rangle/B_0^2$, where $\langle p\rangle$ is the average plasma pressure, μ_0 the vacuum permeability, and B_0 the toroidal magnetic field. The stability of a large class of plasma modes is theoretically limited by this beta normalized by the plasma current, $\beta_N = \beta(aB_0/I)$, where a is the minor radius and I is the toroidal plasma current. How large β_N can be raised to is determined by the stability of the external kink mode [1]. Above a critical value the plasma will disrupt, ending the discharge and possibly damaging plasma-facing components.

1.2 Resistive Wall and Associated Modes

An external wall with finite resistivity plays a major role in the stability of tokamak devices via a variety of mechanisms. Primarily it lowers the stable β_N limit. Any configuration that is unstable to the external kink mode with no wall at all is still ideally unstable with a resistive wall, though the mode growth rate is much slower and can usually be controlled by active feedback systems. When an external kink is moderated by the resistive wall, it is called a resistive wall mode (RWM). Rotation and kinetic effects have been shown

experimentally to be important in passive stabilization of the RWM, but the details are not yet fully understood.

The resistive wall also allows penetration of external error fields into the plasma volume. Even at very small magnitudes, these non-axisymmetric perturbations can affect plasma stability by driving magnetic islands that slow down an otherwise rotating plasma. This could destabilize a RWM by decreasing the rotation, but there might also be nonlinear coupling between the wall and rotating plasma. This report will cover the background in theory, experiment, and computation that has led to our current understanding of RWM stability and associated physics. A thorough review of external kink and RWM stabilization research has also been written by Chu and Okabayashi[2].

1.3 Advantages and Necessity of Simulation

The RWM is analytically simple when approached with ideal linear magnetohydrodynamics (MHD). However, non-linear physics are important in the locked-mode and rotation physics believed to play a part in RWM stabilization. The non-linear extended MHD code NIMROD is an excellent tool for understanding the coupling between the resistive wall, its associated unstable modes, and the plasma rotation. Prior to the research presented in this report, NIMROD had no resistive wall boundary condition.

In this document, we demonstrate the successful implementation and verification of a resistive wall boundary condition for a periodic cylinder. We have also implemented a cylindrical resistive wall and error field boundary condition to demonstrate non-linear mode-locking. Finally, we have implemented a generalized geometry resistive wall boundary condition and tested it for geometries ranging from a simple periodic cylinder to the highly-shaped tokamak NSTX. Numerical convergence studies highlighted some deficiencies in the new boundary condition, but its application to identifying the ideal-MHD RWM

stability limits for NSTX equilibria was moderately successful.

Chapter 2

Background and Theory

2.1 Review of magnetohydrodynamics in tokamaks

2.1.1 Magnetohydrodynamic equations

The magnetohydrodynamic (MHD) equations describe the behavior of conducting fluids such as plasmas. This single-fluid model of a plasma is a good representation of the macroscopic behavior of magnetically confined plasma in fusion energy applications, including the physics of most major instabilities. The resistivity and viscosity of the conducting plasma fluid can also be included, giving the visco-resistive MHD equations. They are [3]:

$$\frac{\partial \rho}{\partial t} + \nabla \cdot (\rho \mathbf{v}) = 0 \quad (2.1)$$

$$\rho \frac{\partial \mathbf{v}}{\partial t} + \rho (\mathbf{v} \cdot \nabla) \mathbf{v} = \mathbf{J} \times \mathbf{B} - \nabla p - \nabla \cdot \rho \nu \nabla \mathbf{v} \quad (2.2)$$

$$\frac{\partial p}{\partial t} + \mathbf{v} \cdot \nabla p = -\gamma p \nabla \cdot \mathbf{v} \quad (2.3)$$

$$\frac{\partial \mathbf{B}}{\partial t} = -\nabla \times \mathbf{E} \quad (2.4)$$

$$\mathbf{E} = -\mathbf{v} \times \mathbf{B} + \eta \mathbf{J} \quad (2.5)$$

$$\mu_0 \mathbf{J} = \nabla \times \mathbf{B} \quad (2.6)$$

$$\nabla \cdot \mathbf{B} = 0 \quad (2.7)$$

where \mathbf{v} is the flow velocity of the single fluid, ρ is the mass density, \mathbf{J} is the current density, \mathbf{B} is the magnetic field, p is the scalar pressure, ν is the viscosity, γ is the ratio of specific heats, \mathbf{E} is the electric field, η is the resistivity, and μ_0 is the permeability of

free space. When diffusive terms are removed ($\nu = 0$, $\eta = 0$), the equations reduce to ideal MHD. In ideal MHD, magnetic fields are frozen into the bulk plasma; this property is known as frozen-in flux. While the resistive terms are small throughout most of the plasma volume in a tokamak, they are comparatively large at a few locations (discussed in the section on tokamak stability) - large enough to break the frozen-in flux condition. This allows for change in the magnetic topology.

2.1.2 Tokamak equilibria

For tokamak operation, the quasi-steady equilibrium is the main factor in determining figures of merit and stability against destructive growing modes. The effects of equilibrium flows can be neglected as long as the flow velocity is less than the ion thermal velocity, which it is in the scope of this report. Then, MHD equilibrium is defined by

$$\mathbf{J} \times \mathbf{B} = \nabla p \quad (2.8)$$

$$\nabla \times \mathbf{B} = \mu_0 \mathbf{J} \quad (2.9)$$

$$\nabla \cdot \mathbf{B} = 0 \quad (2.10)$$

Using a cylindrical coordinate system (R, ϕ, Z) and assuming axisymmetry in the toroidal (ϕ) direction, these give a 2-D equilibrium with nested surfaces of constant flux labeled with the coordinate ψ (related to the poloidal flux, Ψ_{pol}), where

$$\mathbf{B} = B_\phi \mathbf{e}_\phi + \nabla \psi \times \nabla \phi \quad (2.11)$$

$$\Psi_{pol} = 2\pi\psi = \int \mathbf{B}_{pol} \cdot d\mathbf{A} \quad (2.12)$$

From the MHD equilibrium equations, it can be shown that the pressure p and the quantity $F = RB_\phi$ are both functions of ψ , and are therefore also constant on surfaces of constant ψ . Both $p(\psi)$ and $F(\psi)$ must be specified, and then the Grad-Shafranov equation may be

solved to give an equilibrium.

$$\Delta^* \psi = -\mu_0 R^2 \frac{dp}{d\psi} - F \frac{dF}{d\psi} \quad (2.13)$$

$$\Delta^* \psi \equiv R \frac{\partial}{\partial R} \left(\frac{1}{R} \frac{\partial \psi}{\partial R} \right) + \frac{\partial^2 \psi}{\partial Z^2} \quad (2.14)$$

This is a second-order nonlinear elliptic PDE for ψ .

It is often useful to approximate the tokamak as a periodic cylinder with length $L = 2\pi R_0$. Then surfaces of constant flux are simply surfaces of constant radius, r , in the coordinate system (r, θ, ϕ) . In equilibrium, $B_r(r) = 0$, and we can fully specify the equilibrium by choosing two field profiles (such as $B_\theta(r)$ and $B_\phi(r)$.) In the tokamak configuration, the toroidal field, B_ϕ , is dominant, and is often notated as B_0 .

The attributes of a given equilibrium are described by a few parameters, which will be used often in this report. They will be listed with their general definition, and, if applicable, a simplified definition for the periodic cylinder.

- Safety factor q : The safety factor measures the helicity of the magnetic field as a function of r . The safety factor at the center of the nested flux surfaces (called the magnetic axis) is denoted q_0 and has important stability implications. Where q is a rational value, the frozen-in flux condition can be broken by a resonant perturbation which has $m/n = q$, where m and n are poloidal and toroidal mode numbers, respectively.

$$q \equiv \frac{d\Psi_{tor}}{d\Psi_{pol}} = \frac{r B_\phi(r)}{R_0 B_\theta} \quad (2.15)$$

- Magnetic shear s : This is a measure of how the helicity of the magnetic field changes radially.

$$s \equiv \frac{r}{q} \frac{dq}{dr} = 1 - \frac{r}{B_\theta} \frac{dB_\theta}{dr} + \frac{r}{B_\phi} \frac{dB_\phi}{dr} \quad (2.16)$$

- Plasma β : The non-dimensional parameter β measures the balance between the pressure and the magnetic field. Larger β indicates a plasma that is better confined

by the magnetic field.

$$\beta = \frac{2\mu_0 \langle p \rangle}{B_0^2} \quad (2.17)$$

Also useful is β_N , which is normalized to the total plasma current, I , and the minor radius, a .

$$\beta_N = \beta \frac{aB_0}{I} \quad (2.18)$$

- Alfvén velocity, V_A , and Alfvén time, τ_A : the primary MHD wave in a compressionless plasma is the Alfvén wave, the dispersion relation of which is $\omega = k_{\parallel} V_A$. The Alfvén parameters are often used as normalization factors, because they capture the most basic velocity and time scales of the plasma. Here, a is the minor radius of the tokamak, though it can be generalized to the global length scale of any experiment.

$$V_A = \frac{B_0}{\sqrt{\mu_0 \rho}} \quad (2.19)$$

$$\tau_A = a \frac{\sqrt{\mu_0 \rho}}{B_0} \quad (2.20)$$

- Hydromagnetic time scale τ_H : At a resonant surface, $k_{\parallel} = 0$, so the wave that defines the Alfvén time cannot propagate, and τ_A is not the best parameter to use. Following the formalism of Fitzpatrick[4], we introduce a hydromagnetic time scale that is still valid at the rational surface. It is of the same order as the global Alfvén time.

$$\tau_H = \frac{R_0}{B_{\phi}} \frac{\sqrt{\mu_0 \rho}}{ns} \quad (2.21)$$

- The resistive and viscous time-scales (τ_R , and τ_V): these time scales are specified at a specific radial location, r_s . These are defined as:

$$\tau_R = \frac{\mu_0}{\eta(r_s)} r_s^2 \quad (2.22)$$

$$\tau_V = \frac{r_s^2}{\nu(r_s)} \quad (2.23)$$

- Lundquist number S : A dimensionless parameter measuring the resistivity of the plasma (small S denotes large resistivity and vice versa.)

$$S = \frac{\tau_R}{\tau_A} \sim \frac{\tau_R}{\tau_H} \quad (2.24)$$

- Magnetic Prandtl number P : A dimensionless parameter of the ratio of viscous to resistive diffusion.

$$P = \frac{\tau_R}{\tau_V} = \frac{\nu}{\eta/\mu_0} \quad (2.25)$$

2.2 Kink and resistive wall instabilities

2.2.1 Theory of kink instabilities

The stability of a plasma surrounded by a vacuum can be determined using the energy principle developed by Bernstein *et al* [5]. Using the ideal MHD equations, the availability of free energy for driving an instability is given by δW . With equilibrium current density \mathbf{J}_0 , equilibrium pressure p_0 , a perturbed magnetic field \mathbf{b} , and a plasma displacement ξ , δW is defined as

$$\delta W = \delta W_{plasma} + \delta W_{vacuum} \quad (2.26)$$

$$\delta W_p = \frac{1}{2} \int_{plasma} \left[\frac{\mathbf{b}^2}{\mu_0} - \mathbf{J}_0 \cdot (\mathbf{b} \times \xi) + \gamma p_0 (\nabla \cdot \xi)^2 + (\xi \cdot \nabla p_0) \nabla \cdot \xi \right] d^3x \quad (2.27)$$

$$\delta W_v = \int_{vacuum} \frac{\mathbf{b}^2}{2\mu_0} d^3x \quad (2.28)$$

An equilibrium is stable to ideal MHD instabilities if $\delta W > 0$ for any displacement ξ . In the plasma, the perturbed magnetic field is related to the plasma displacement by $\mathbf{b} = \nabla \times (\xi \times \mathbf{B}_0)$. The formulation above assumes that the vacuum itself is surrounded by a perfectly conducting wall. If the wall is adjacent to the plasma (with no vacuum between plasma and wall,) and $\delta W < 0$, then the plasma is unstable to an internal mode. If an equilibrium is stable with a wall adjacent to the plasma, but unstable with a vacuum

between the wall and the plasma, the mode is external, in that it requires a magnetic perturbation in the vacuum. The most prominent of these is the external kink mode (XK). Troyon theorized that the stability of the XK leads to a maximum allowable value of β_N [6]. He predicted that $\beta_{N,max} = 2.8$.

2.2.2 Theory of resistive wall instabilities

It is important to consider the addition of a physically realistic resistive wall to the system. Adding a second, resistive wall interior to the perfectly conducting wall may change some features of the instability, but, as was shown by Pfirsch and Tasso, it cannot stabilize an unstable system[7]. Replacing the perfectly conducting wall with a resistive wall leaves the system unstable to any modes which are unstable for the no-wall scenario, though the resulting resistive wall modes (RWMs) will have growth times on the scale of the wall resistive diffusion time, which is, in general, much longer than the characteristic MHD time scale. The hydromagnetic time scale, given by Eq.(2.21), is of order 10^{-6} seconds, while the wall time, given by Eq.(2.29), is of order 10^{-2} seconds for thin stainless steel metal.

$$\tau_{wall} = \frac{\mu_0 \delta_w r_w}{\eta_w} \quad (2.29)$$

This time scale separation is useful, as the resistive wall slows external modes to growth rates which are more easily controlled by an external feedback mechanism.

The derivation of the resistive wall growth rate and eigenfunctions is demonstrated in more detail for a periodic cylinder with an analytically simple equilibrium in Section 3.2.

2.2.3 The vertical displacement event: a particularly nasty case of the RWM

One important manifestation of the RWM is a vertical instability of the plasma column which can lead to a vertical displacement event (VDE), a disruption that terminates the

plasma discharge. To maintain plasmas with high β and large plasma current I_p , shaping fields are used to create optimized vertically elongated plasma shapes. Plasma columns with vertical shaping are unstable to an $n = 0$ mode, during which a small vertical displacement Δz leads to a force that enforces the displacement. If this instability goes uncontrolled, the plasma column will be quickly forced into either the top or the bottom of the vacuum chamber. Not only is the discharge halted, but the VDE causes large, often damaging, thermal loads on the wall and large electromagnetic forces on external structures, up to 350 tons in JET[8].

Passive control structures, such as a resistive wall, cannot prevent a VDE in an otherwise vertically unstable plasma, but they can slow the growth of the initial instability to the scale of the wall time. The mode is then growing slowly enough that it can usually be stabilized by active feedback control. Experimental and numerical results show that the growth rates of vertical instabilities are proportional to the wall resistivity[8, 9, 10].

2.2.4 Advancements in the understanding of RWM stability

Initial experimental studies of the XK tested the validity of the Troyon scaling theory. Experiments at the DIII-D[11] and PBX [12] tokamaks showed that the scaling theory was valid, but that the maximum value of β_N was higher than predicted, at 3.5 (instead of 2.8,) with the difference being attributable to the external conducting wall that provides a stabilizing effect.

In experiments performed on TFTR[13], it was shown that the growth rates of the modes responsible for the β -limit did not match the rates predicted by the ideal MHD model with no external wall. Experimental growth rates were often significantly lower than predicted. When further experiments in the 1990s demonstrated that slower-than-expected growth rates in rotating plasmas were even lower than the inverse wall time, a theoretical model with more physics was needed to explain the plasma behavior.

Bondeson and Ward provided insight by demonstrating RWM stabilization for $\beta_N > \beta_{N,max}$ in a simulation of a dissipative toroidal plasma with a rotating wall[14]. Theorists then attempted to flesh out these results with a robust analytic theory. Betti and Freidberg showed that resonance of the RWM with the sound wave continuum could produce the dissipation needed (along with rotation) for stabilization[15]. This analysis was performed for a cylinder, but it was shown that toroidal effects increased the stabilizing dissipation. Fitzpatrick and Aydemir developed a cylindrical model in which the dissipation was provided by edge plasma viscosity[16]. Although the physical causes are different, the Betti-Freidberg and Fitzpatrick-Aydemir models both predict critical rotation velocities an order of magnitude smaller than the Alfvén speed and a RWM dispersion relation that is cubic in γ . Hu and Betti modified the δW formulation to include kinetic effects (but an otherwise ideal plasma), with a dispersion relation written in terms of the free energy with no wall, δW_∞ , the free energy with a wall at r_w , δW_{r_w} , and a term accounting for kinetic effects, δW_K .

$$\gamma\tau_w = -\frac{\delta W_\infty + \delta W_K}{\delta W_{r_w} + \delta W_K} \quad (2.30)$$

The critical rotation threshold at which the RWM is stabilized seems to be dependent (in theory and experiment) on how the rotation is reached. One method is to use a symmetry-breaking perturbation to slow a quickly rotating plasma through magnetic braking. When this method is used, critical rotation frequencies of $\Omega_{crit}\tau_A \sim 1\% - 2\%$ are found in DIII-D[17] and JT-60U[18]. The other method for reaching the desired rotation is by using small torque input (i.e. using neutral beam injection with one beam directed counter to the plasma current) while reducing error fields that might brake the plasma rotation. More recent experiments on DIII-D[19] and JT-60U[20] have observed critical rotation speeds for RWM stabilization of 0.3% of the Alfvén speed using this method, which minimizes magnetic braking. The different results from these two methods are best

explained by considering the balance between the electromagnetic torque from a perturbation and the viscous torque, as proposed by Jensen *et al*[21] and Fitzpatrick[22]. In certain regimes there is a bifurcation point in the torque balance equation in the presence of an error field, which can cause a sharp transition from large to small plasma rotation, or vice versa (though the transition from small to large rotation occurs at a different point.) When a resonant error field is used to slow the plasma rotation, it cannot slow it enough without reaching the bifurcation point, locking, and destabilizing the RWM. When the torque is controlled by changing the injected momentum instead, no bifurcation point occurs, and the rotation can be lowered smoothly to the actual stability threshold. The details and derivation of torque balance and bifurcation will be addressed in Section 2.3.3. Experiments on DIII-D confirm the viability of this theory[23].

2.3 Magnetic error fields or perturbations

Small perturbations on the background equilibrium magnetic field are always present in experimental devices. Sometimes they are applied intentionally by a specific set of coils (such as the I- or C-Coils at DIII-D[24, 25]) to mitigate edge localized modes (ELMs)[26] or to drive a particular mode to study it. Invariably, misalignments in the coils that produce the equilibrium magnetic fields will also produce small perturbations on those fields, called error fields (EFs.) These fields can interact in various ways with the plasma and its instabilities. They can drive magnetic islands which flatten temperature and pressure gradients and can slow a rotating plasma, sometimes locking it to the wall. Slowing the plasma rotation too much can destabilize RWMs, as discussed in the previous section.

2.3.1 Review of basic island and tearing mode physics

To understand the main effect of error fields on the plasma, one must first have a grasp on the physics of tearing modes and the magnetic islands associated with them. For a perturbation with wave vector $\mathbf{k} = m\mathbf{e}_\theta - n/R\mathbf{e}_\phi$, there may exist a rational surface in the plasma where $\mathbf{k} \cdot \mathbf{B} = 0$ and $q = m/n$. At this rational surface, q_s , at radius r_s , the resistive diffusion term in the induction equation becomes non-negligible, and the frozen-in flux condition is broken. This allows change to the magnetic topology; instead of being nested, flux surfaces can cross, forming a chain of magnetic islands that winds around the device.

In our analysis of the tearing-mode problem, we'll consider magnetic perturbations of the form

$$\mathbf{b} = \nabla\psi \times \mathbf{e}_z \quad (2.31)$$

where ψ is the flux. Let us examine the radial component of the induction equation:

$$\frac{\partial}{\partial t} b_r = \mathbf{e}_r \cdot \nabla \times (\mathbf{v} \times \mathbf{B}) + \frac{\eta}{\mu_0} \nabla^2 b_r \quad (2.32)$$

where upper-case quantities are equilibrium values and lower case quantities are perturbed values. For perturbed values proportional to $e^{(\gamma t + m\theta - n\phi)}$ and writing b_r in terms of ψ , this can be simplified to

$$im\gamma \frac{\psi}{r} = \frac{B_\theta}{r} (m - nq)v_r + im \frac{\eta}{\mu_0} \nabla^2 \frac{\psi}{r} \quad (2.33)$$

Integrating radially across the rational surface's resistive layer of width δ_s where b_r is constant but its derivative is discontinuous, gives a condition for tearing mode stability.

For this short radial extent $\nabla^2 \sim \partial^2/\partial r^2$ and b_r is constant.

$$\gamma\tau_s\psi(r_s) = r_s \left[\frac{\partial}{\partial r} \psi \right]_{r_s} \quad (2.34)$$

$$\tau_s = \frac{\mu_0}{\eta} r_s \delta_s \quad (2.35)$$

$$\Delta' \equiv \frac{r_s}{\psi(r_s)} \left[\frac{\partial}{\partial r} \psi \right]_{r_s} \quad (2.36)$$

The conditional for marginality is $\Delta' = 0$, and $\Delta' > 0$ indicates instability. This is determined by the plasma equilibrium and geometry. The layer width δ_s is a function of the plasma properties within the resistive layer, and can be found using asymptotic matching of the linear equations, as outlined by Fitzpatrick[27]. This layer width depends on the plasma parameters, and the equation defining it is also dependent on what physics are dominant for a given set of parameters. Generally, plasma viscosity, resistivity, and inertia can play a role in determining layer width, though at least one of these factors is negligible in a given regime. We will be considering plasmas in the visco-resistive regime, where the inertia in the layer is negligible, and the layer width is[4]

$$\delta_s = r_s \left(\frac{\tau_H^2}{\tau_{RTV}} \right)^{1/6} \quad (2.37)$$

where all times are evaluated in the layer. Linear layer theory is only valid when the island width, W_s , is smaller than than the layer width, δ_s . The width is defined as the radial extent of the magnetic separatrix where the magnetic topology changes from well-nested to island-like.

$$W_s = 4 \sqrt{\frac{b_r(r_s)r_s}{B_\theta(r_s)q'n}} \quad (2.38)$$

When $\delta_s \sim W_s$ the mode transitions from linear growth (during which $b_r \sim e^{\gamma t}$) to non-linear behavior. Locally, the $\mathbf{j} \times \mathbf{b}$ force becomes comparable and opposite to the $\mathbf{j} \times \mathbf{B}$ force, leading to saturation of the island amplitude. This theory was developed by Rutherford[28]. The linear and Rutherford theories make the assumption that ψ is constant across the resonant surface. Further physics is required when ψ is non-constant across the tearing layer: this is addressed by Waelbroeck[29, 30].

The initial formation of islands in a tearing-mode unstable plasma is a current area of research, and is not within the scope of this work. We will be considering only islands driven by error fields.

2.3.2 Theory of error field driven islands

One can Fourier decompose error fields poloidally (m) and toroidally (n) to give the field's harmonic spectrum. This resonant component of the field can then drive an island at the $q_s = m/n$ surface, where the resistivity becomes important and the frozen-in flux condition is broken, even if the plasma is otherwise stable to tearing modes (where $\Delta' < 0$.) While the flux ψ is constrained to be zero at the wall for an ideal wall, one can consider an additional ψ (and b_r) at the wall due to an error field. This changes the boundary conditions on Eq. (2.33) and gives a different b_r eigenfunction, and thereby changes Δ' . First, we consider how an error field at the boundary would penetrate into a vacuum. We can find the vacuum eigenfunction by solving $\nabla \times \mathbf{b} = 0$ with the appropriate boundary conditions. For a periodic cylinder, this gives

$$\psi_{vac} = \Psi_v \left(\frac{r}{r_s} \right)^m \quad (2.39)$$

where Ψ_v is the value of the perturbed flux at the rational surface in a vacuum. A non-zero b_r at a resonant rational surface produces a vacuum magnetic island. However, this does not capture what happens when an error field penetrates into a plasma. Consider a perturbed flux composed of the plasma tearing response, ψ_{plasma} , governed by Eq. (2.34) and the ideal MHD response to the error field, $\psi_{shielded}$, which is 0 at $r \leq r_s$ and $\psi_{vac}(r_w)$ at the wall.

$$\psi_{tot} = \psi_p + \psi_{sh} \quad (2.40)$$

$$\psi_{sh} \simeq \Psi_v \left[\left(\frac{r}{r_s} \right)^m - \left(\frac{r}{r_s} \right)^{-m} \right] \quad (2.41)$$

$$r_s \left[\left[\frac{\partial \psi_{tot}}{\partial r} \right] \right]_{r_s} = \psi_{pl} \Delta' r_s + 2m \Psi_v \quad (2.42)$$

Since we're considering cases that are stable to growing tearing modes, but may have some intrinsic rotation, we consider perturbed fields $\propto e^{i\omega t}$ instead of $\propto e^{\gamma t}$. Now, combining

Eq. (2.34) and Eq. (2.42) for a rotating, stable plasma, we arrive at an equation for Ψ_s , the amplitude of the plasma response to the error field at the magnetic surface.

$$\Psi_s = \psi_{pl}(r_s) = \frac{2m}{-\Delta' + i\omega\tau_s} \Psi_v \quad (2.43)$$

When there is no plasma rotation and $\omega = 0$, Ψ_s is larger than Ψ_v , since, generally, $-\Delta' < 2m$. This phenomenon is known as resonant field amplification (RFA.) If, instead, the rotation is large compared to the inverse layer time, the rotation can sustain a current sheet at the rational surface that suppresses magnetic reconnection and forces Ψ_s to 0. This is referred to as the plasma shielding the error field. A more general theory for RFA is the lumped parameter model introduced by Okabayashi *et al*[31] and expanded upon by Boozer[32]. The plasma, wall, and error field are represented by circuit components, such that

$$L_{eff}I_p + M_{pw}I_w + M_{pc}I_c = 0 \quad (2.44)$$

$$\frac{\partial}{\partial t} (M_{wp}I_p + L_wI_w + M_{wc}I_c) + R_wI_w = 0 \quad (2.45)$$

where I_p , I_w , and I_c are the currents in the plasma, wall, and error field respectively, L_{eff} is the effective plasma inductance, and R_w is the resistance of the wall. $M_{i,j}$ is the mutual inductance between the various currents.

2.3.3 Torque balance and mode-locking theory

Both RFA and plasma shielding take into account only the linear plasma response to the error field. The importance of non-linear effects is evident in the torque balance equation. In normal tokamak operation, poloidal rotation is damped away due to strong parallel viscosity. Therefore, while our derivation begins with T_ϕ , the torque acting on the poloidal rotation, we will consider the torque balance in the toroidal direction (The following theory has been generalized to include torque balance on the poloidal flow as

well, as seen in Section 4.4.) The flux-surface-averaged non-linear electromagnetic poloidal torque at radius r_s is given by

$$T_{EM,\phi} = \oint \oint r_s (j_\phi b_r^* + j_\phi^* b_r) r_s d\theta R_0 d\phi \quad (2.46)$$

$$= -\frac{2\pi^2 r_s R_0 m}{\mu_0} \Im(\nabla^2 \psi \psi^*) \quad (2.47)$$

We can then integrate over the layer width to determine the total poloidal EM torque as a function of the mode rotation, tearing stability, layer characteristics, and applied error field. Applying Eqs (2.34, 2.43) to Eq. (2.47) and using integration by parts gives

$$T_{EM,\phi} = -\frac{8\pi^2 R_0 m^3}{\mu_0} \frac{\omega \tau_s}{(-\Delta')^2 + (\omega \tau_s)^2} |\Psi_v|^2 \quad (2.48)$$

Thus, the electromagnetic torque from the error field varies non-monotonically with the rotational frequency of the mode. Although our representation of the perturbed current neglects all but the toroidal current, we can relate the poloidal current in the resistive layer to the toroidal current in the layer, by noting that $\nabla \cdot \mathbf{j} = 0$, leading to the conclusions that

$$\frac{m}{r} j_\theta - \frac{n}{R_0} j_\phi = 0 \quad (2.49)$$

$$T_{EM,Z} = -\frac{n}{m} T_{EM,\phi} = \frac{8\pi^2 n m^2 R_0}{\mu_0} \frac{\omega \tau_s}{(-\Delta')^2 + (\omega \tau_s)^2} |\Psi_v|^2 \quad (2.50)$$

This torque acts in such a way as to decrease the total rotation. The other main contribution to the torque is the viscous restoring force. This force opposes change in the rotation. Following a similar method as was used for the electromagnetic torque, we find the viscous torque on the toroidal rotation to be

$$T_{VS,Z} = 4\pi^2 R_0^3 r_s \rho \nu \left[\left[\frac{d\Delta \Omega_\phi}{dr} \right] \right]_{r_s} \quad (2.51)$$

As outlined by Fitzpatrick[4], it is assumed that at all radial locations except the rational surface, the viscosity acts to return the rotation to its unperturbed level, and that this is

essentially steady state. This is stated as

$$\frac{d}{dr} \left(r \rho \nu \frac{d\Delta\Omega_\phi}{dr} \right) = 0 \quad (2.52)$$

We take the rotation at the edge of the plasma to be unchanged, and can then find $\Delta\Omega_\phi$ in all regions of the plasma.

$$\Delta\Omega_\phi(r) = \begin{cases} \Delta\Omega_\phi(r_s) & 0 < r < r_s \\ \Delta\Omega_\phi(r_s) \left(\int_r^{r_w} \frac{dr}{r\rho\nu} \right) / \left(\int_{r_s}^{r_w} \frac{dr}{r\rho\nu} \right) & r_s < r < r_w \end{cases} \quad (2.53)$$

It follows that this torque acts to minimize the change in rotation, as

$$T_{VS,Z} = - \frac{4\pi^2 R_0^3 \Delta\Omega_{\phi,s}}{\int_{r_s}^{r_w} \frac{dr}{r\rho\nu}} \quad (2.54)$$

The total mode rotation, ω , includes any initial (or equilibrium) rotation, ω_0 , plus the contribution of $\Delta\Omega$.

$$\omega_0 = m\Omega_{\theta,0}(r_s) - n\Omega_{\phi,0}(r_s) \quad (2.55)$$

$$\omega = \omega_0 - n\Delta\Omega_{\phi,s} \quad (2.56)$$

We can combine this definition of the mode rotation with the equations for the electromagnetic and viscous torques to give

$$T_{EM,Z} + T_{VS,Z} = 0 \quad (2.57)$$

$$\frac{2n^2 m^2 \tau_s \left(\int_{r_s}^{r_w} \frac{dr}{r\rho\nu} \right) |\Psi_v|^2}{\mu_0 R_0^2 (-\Delta')^2} \frac{\omega}{(1 + (\omega\tau_s/(-\Delta'))^2)} = \omega_0 - \omega \quad (2.58)$$

To see the physical importance of this equations, we can make a few simplifications. First, we define a modified layer time $\tau_s^* = \tau_s/(-\Delta')$. We can define A , related to the error field amplitude such that

$$A = \frac{2n^2 m^2 \tau_s \left(\int_{r_s}^{r_w} \frac{dr}{r\rho\nu} \right) |\Psi_v|^2}{\mu_0 R_0^2 (-\Delta')^2} \quad (2.59)$$

$$A = \frac{\omega_0}{\omega} - 1 + \omega_0 \omega \tau_s^{*2} - \omega^2 \tau_s^{*2} \quad (2.60)$$

Critical values of the rotation occur when $dA/d\omega = 0$. This equation is cubic, and mode-locking occurs when all three roots are real and distinct (as shown in Fig 1a,) when the discriminant of the cubic is > 0 [33]. This provides us with a minimal critical initial rotation ω_0 required for an abrupt mode-locking. If $\omega_0 < \omega_{0,crit}$, then the total rotation is never large enough to maintain a sheet current at the rational surface and shield the plasma from the error field. In this case, the error field will smoothly slow the plasma down. If $\omega_0 > \omega_{0,crit}$, there are two branches: a large rotation solution and a small rotation solution.

$$\omega_{0,crit} = \frac{3\sqrt{3}}{\tau_s^*} \quad (2.61)$$

If an error field is increased in time from 0, the mode will slow until it reaches the

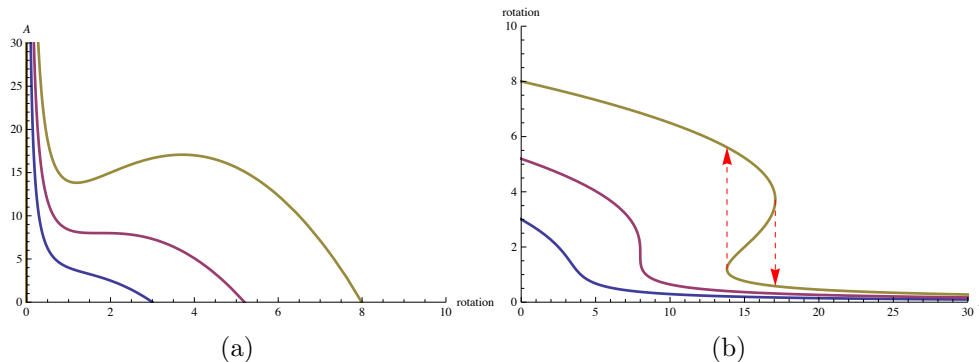


Figure 1: (a) Normalized error field amplitude A as a function of total plasma rotation for initial rotation from large (yellow) to small (blue). (b) Rotation as a function of normalized error field amplitude A . Dotted arrows indicate downward and upward jumps between small and large rotation solutions for a bifurcated system.

bifurcation point, at which point it will quickly jump to the slowly rotating solution. If the error field is then decreased in time, the rotation will slowly ramp up until it reaches a different bifurcation point, at which point it will quickly jump to the quickly rotation solution. This behavior is shown for an analytical case in Fig 1b. This curve is the same as that of Fig 1a, but with the axes switched.

The downward bifurcation point occurs at $\omega = \omega_0/2$ for the visco-resistive regime[4].

Knowing this, it is simple to calculate the applied error field $|\Psi_v|$ required to lock the mode when in the bifurcating regime.

$$|\Psi_v| = \frac{\omega_0 R_0}{2nm} \sqrt{\frac{\mu_0 \tau_s}{2 \int_{r_s}^{r_w} (dr/r\rho\nu)}} \quad (2.62)$$

The radial magnetic field at rational surface in the absence of plasma is related to $|\Psi_v|$ by

$$\mathbf{b}_r = \frac{m|\Psi_v|}{r_s} \quad (2.63)$$

The form of the torque balance equation is dependent on what layer regime best describes the resonant surface. Fitzpatrick[4] has shown the analysis for a variety of regimes and gives their characteristic layer widths, critical rotations, and bifurcation points.

2.3.4 The effects of error fields in experiment

Error fields and their effect on rotation and the RWM can be studied by applying known perturbed fields and using magnetic probes and flux loops to measure the plasma response. The DIII-D tokamak has two sets of coils that can be used to apply a specified magnetic perturbation external to the plasma[24, 25]. The C-coils are external to the vacuum vessel and include six coils evenly spaced around the outboard side with symmetry about the midplane. These can produce a field with the most prominent harmonic at $m = 1$, but, due to their up-down symmetry, no helicity. The I-coils are internal to the vacuum vessel and consist of 6 evenly spaced coils above the midplane and 6 evenly spaced coils below the midplane, all on the outboard side. The helicity of the applied field can be changed by changing the phase of the signal between the upper and lower set of coils. These are typically used such that the strongest harmonic is the $m/n = 3/1$ component, since it is expected to be the dominant helicity for RWMs. However, the spectrum of the applied field is broad enough that the resonant eigenmodes of the plasma play an equally important role in determining what harmonics are excited. These sets of coils can be used both to

purposefully destabilize the system and to correct inherent error fields in the experiment. The first experiments to measure RFA were done at DIII-D using the C-coils to apply an $n=1$ field to the plasma[34]. Radial flux loops measure the field near the surface, and the amplification is quantified as

$$A_{RFA} = (B_r - B_{r,vac}) / B_{r,vac} \quad (2.64)$$

It was shown that the A_{RFA} was larger when $\beta_N > \beta_{N,crit}$. Similar results were obtained at JET[35] and NSTX[36]. Experiments at COMPASS-D observed plasma equilibria with a resistive wall and a magnetic island that were rotating at either a high or a low frequency[37]. The band of forbidden rotation frequencies was consistent with the theory of torque balance presented above. The bifurcated nature of the torque balance in rotating system with an error field was also studied experimentally in a line-tied screw pinch with a rotating wall by Paz-Soldan[38]. In this case the driven mode was a kink rather than a tearing mode, though a similar layer analysis can be used at the plasma surface, as is demonstrated by Fitzpatrick [22]. As discussed in Section 2.2.4, the bifurcation between a locked and unlocked plasma in the presence of error fields plays an important roll in the rotational stabilization of the RWM.

2.4 Numerical implementations of a resistive wall and error fields

Numerical studies of tokamak plasmas expand the field of research beyond what is analytically tractable and provide a window into the complicated plasma dynamics that are difficult to measure in experiment. However, no single code perfectly models the complexities of the real world. Only a certain amount of the physical system can be represented at once, and a variety of numerical methods are used by plasma codes in order to most

efficiently simulate the physical properties to be studied.

2.4.1 Codes for studying XK stability

With the initial interest in tokamak stability came the creation of codes to study ideal MHD stability. These include ERATO[39], PEST[40], GATO [41], and DCON[42]. These codes are useful for understanding the underlying XK instability which is modified by the wall to create a RWM. They do not include the ability to model a system with a resistive wall; their boundary conditions are either free or a perfectly conducting wall. ERATO was used in the discovery of the Troyon β scaling law[6]. Troyon used a JET-like plasma shape and varied q_0 and β while keeping the current I constant.

2.4.2 The MARS code

MARS[43] and its extensions have made many important contributions to our understanding of the RWM. It is a linearized MHD eigenvalue code in toroidal geometry that includes flow. Bondeson and Ward's hypothesis that rotation stabilized the RWM via ion Landau damping was supported by numerical results from MARS[14]. MARS has since been extended to include magnetic feedback (in MARS-F[44]) to study active control of RWMs. The extension MARS-K[45] includes drift kinetic terms in the perturbed pressure tensor, and can be used for numerical comparison to the kinetic stabilization theory of Hu and Betti[46], which includes bounce, transit, diamagnetic, and magnetic drift resonances. MARS reliably predicts RWM stability thresholds in rotation for DIII-D, so long as error fields are minimized and a low torque input is used to reach the desired rotation[23]. Another use of MARS for RWM study has been in the CarMa code[47], in which it is coupled with the 3D eddy current code CARIDDI[48]. CarMa was used to predict that ITER's proposed thick blanket modules (which would have volumetric eddy currents) could reduce the RWM growth rate by approximately 20%[49]. The VALEN code [50] also uses output (a

plasma permeability matrix) from either MARS or DCON as input to determine the complex effects of external structures on plasma stability.

2.4.3 The M3D and M3D-C1 codes

M3D (Multilevel 3D) aims to model a more realistic plasma by using a hierarchy of physics models including fluid and hybrid-kinetic models[51]. It is a nonlinear code. A resistive wall (with non-trivial shaping in the poloidal plane) was added by matching the plasma magnetic field solution with a vacuum magnetic field produced by the GRIN code[52]. The resistive wall functionality was used by Strauss *et al*[9] to study VDEs (as discussed in Section 2.2.3.) Based on similar design principles, the two-fluid, finite element resistive MHD code M3D-C1[53] can be used to study error fields and the effects of the resistive wall. The method used to model the resistive wall is different from the one used in this work, with a wall of finite thickness and a vacuum region outside the wall all part of the computational domain[54].

2.4.4 The AEGIS code

A resistive wall is included in the linear code AEGIS[55], which uses an adaptive shooting method in the radial direction, rather than the more commonly used finite element method. AEGIS was used by Zheng *et al* to demonstrate that finite δ_w reduces the growth rate of the RWM[56]. The AEGIS-K code solves the gyrokinetic equations with a resistive wall[57] and recovers both MHD and finite Larmor radius effects in their respective limits.

2.4.5 The coupled JOREK and STARWALL codes

JOREK is a non-linear reduced MHD code[58]. It is being extended to include a resistive wall by coupling it to the vacuum field solver STARWALL[59]. STARWALL makes the

thin shell approximation but planned code development will allow for walls that are non-axisymmetric and have holes. JOREK with a resistive wall via STARWALL has shown analytically predicted RWM linear growth-rate dependency on wall radius and resistivity for a toroidal geometry with a circular plasma cross-section. Non-linear runs show RWM saturation when wall currents in the high-field side have an amplitude comparable to those in the low-field side[59].

2.4.6 Codes with external magnetic perturbations but no resistive wall

There are a few codes that model plasma with an applied external perturbation that do not include a resistive wall. For instance, the ideal MHD code IPEC[60] models the plasma response to an external perturbation applied as a boundary condition, without allowing reconnection. However, this boundary condition does not respond to the plasma currents, as would be the case with a resistive wall.

2.5 Overview of the NIMROD code

The code NIMROD (Non-Ideal Magnetohydrodynamics with Rotation, Open Discussion) evolves the MHD equations with user-specified closures[61]. This can be done in a variety of geometries, including axially periodic slab and cylindrical systems, as well as the experimentally relevant toroidal system. The poloidal plane is discretized using 2D spectral elements, and the periodic (axial) direction is represented using a finite Fourier series. Instead of including $\nabla \cdot \mathbf{B} = 0$ in the system of equations being solved, the divergence error is kept small using an artificial diffusion term in Faraday's law, where κ_{divB} is a user-specified parameter to set the strength of the diffusion. In addition, an artificial density diffusion with coefficient D is included in the continuity equation to maintain smooth density profiles. Shown here is a representative system of NIMROD equations with kinematic

viscous dissipation.

$$\frac{\partial n}{\partial t} + \nabla \cdot (n\mathbf{v}) = \nabla \cdot D\nabla n \quad (2.65)$$

$$\rho \frac{\partial \mathbf{v}}{\partial t} + \rho(\mathbf{v} \cdot \nabla)\mathbf{v} = \mathbf{J} \times \mathbf{B} - \nabla p + \nabla \cdot \nu \rho \nabla \mathbf{v} \quad (2.66)$$

$$\frac{n}{\gamma - 1} \left(\frac{\partial T}{\partial t} + \mathbf{v} \cdot \nabla T \right) = -\frac{p}{2} \nabla \cdot \mathbf{v} - \nabla \cdot \mathbf{q} + Q \quad (2.67)$$

$$\frac{\partial \mathbf{B}}{\partial t} = -\nabla \times \mathbf{E} + \kappa_{divB} \nabla \nabla \cdot \mathbf{B} \quad (2.68)$$

$$\mathbf{E} = -\mathbf{v} \times \mathbf{B} + \eta \mathbf{J} \quad (2.69)$$

$$\mu_0 \mathbf{J} = \nabla \times \mathbf{B} \quad (2.70)$$

All evolved variables are stored as the sum of a steady-state equilibrium value and a time-evolving perturbation. This is done because meaningful perturbations can be many orders of magnitude smaller than the equilibrium value, and because sources used to maintain the equilibrium can be disregarded in the plasma evolution. NIMROD can be run either linearly (using terms with only one perturbed quantity contribution) or non-linearly (including terms with multiple perturbed quantities.) Because of the large range of time scales important to the evolution of a plasma, NIMROD uses a semi-implicit leap-frog method to advance variables in time. The velocity is advanced at integer time steps using a semi-implicit operator, while the magnetic field, density, and temperature are advanced at half-integer time steps. The electric field and current can then be determined in post-processing and used to gain a better understanding of the physical effects being modeled.

The standard boundary conditions for NIMROD are that of a conducting wall (which enforces time-independent normal magnetic field at the wall) and no-slip velocity boundary conditions (enforcing that all components of the perturbed velocity are zero at the wall.) Previous additions to the basic boundary conditions have included an external loop voltage applied via the wall and resonant magnetic perturbations (RMPs) imposed at the

wall. The primary focus of the research documented in this report has been to expand the magnetic boundary conditions to include a cylindrical resistive wall (Chapter 3), a cylindrical resistive wall with external error fields (Chapter 4), and a resistive wall for a more general toroidal geometry (Chapter 5).

2.5.1 Equilibria for NIMROD

The pre-processing utility `nimset` creates the computational grid, sets initial perturbations, and sets the equilibrium profiles. For a cylindrical geometry, the basic equilibrium can be set by choosing from built-in pressure and q profiles and setting the various parameters associated with them, including the axial magnetic field on-axis and β . Instead of the q -profile, `nimset` also includes the functionality to specify a pitch or lambda profile. For toroidal geometries, the code TOQ[62] can be used to generate a suitable magnetic configuration for circular cross-sections. TOQ is an inverse equilibrium solver, and its equilibrium solutions are only applicable to regions where magnetic surfaces of constant ψ are simply nested closed contours. For irregular cross-sections, such as the familiar D-shape favored by many modern tokamaks, the pre-processing utility `fluxgrid` can take flux-surface shapes and quantities from equilibrium reconstruction codes such as EFIT and create and fill flux-aligned grids.

2.5.2 Spectral elements and Fourier representation of quantities

As stated previously, NIMROD uses a truncated Fourier series in the axial direction. All spatially dependent fields are represented as

$$Q = Q_0 + \sum_{n=1}^N \left[Q_n e^{in\phi} + Q_n^* e^{-in\phi} \right] \quad (2.71)$$

where Q represents scalar fields or components of vector fields, N is a user-specified truncation point for the series, and $*$ represents a quantity's complex conjugate. The quantity

Q represents a physical quantity, and is, by definition, real. Q_n and Q_n^* are complex. NIMROD only performs computations with Q_n ; finding its complex conjugate is trivial. It should be noted that NIMROD results are for perturbations that behave as $e^{in\phi}$, while most physics calculations (especially those considering rational surfaces with positive m , n , and q ,) consider perturbed quantities proportional to $e^{-in\phi}$. Therefore, in the resistive wall calculations discussed in Chapter 3, the possibility of $-m$ must be considered.

In the poloidal plane, the physical coordinates (R, Z) are mapped to logical coordinates (η, ξ) to facilitate grid-packing in real space so that regions with large gradients can be resolved. This mapping is defined in each (η, ξ) element. As seen in Eq.(2.72), the Fourier coefficient quantities Q_n can be expanded on a set of finite element basis functions α_j . These are products of low order polynomials in η and ξ that span limited regions of the domain.

$$Q_n(R, Z) = \sum_j \alpha_j(\eta, \xi) Q_{jn} \quad (2.72)$$

NIMROD utilizes the Galerkin method: equations are converted to their weak form by multiplying by a test function α_i , from the same set of basis functions used in the finite element decomposition, and integrating over the total volume. The surface contributions from interior elements cancel each other out, and the only surface contribution is from the boundary of the computational domain. Faraday's law written in this form - Eq.(3.2) - will be used in Section 3.1, and a practical example of putting an equation in weak form and why this is advantageous can be found in Section 5.1.

Chapter 3

Resistive wall boundary condition for a periodic cylinder

The basis of all subsequent work was the development, implementation, and testing of a resistive wall boundary condition for a periodic cylinder in NIMROD. It provided the basic code mechanism for the error field studies in Chapter 4 and the experience with RWM behavior (both physically and numerically) necessary to tackle the challenges of implementing a resistive wall boundary condition for a more general geometry in Chapter 5.

3.1 Implementation in NIMROD

The resistive wall boundary condition is applied by specifying the surface electric field in the wall as a surface term in the induction equation. The semi-implicit spectral element form of the induction equation used by NIMROD is shown in Eq.(3.2), for all \vec{A}_i in the space of functions for $\Delta\vec{B}$. The explicit electric field on the right-hand-side (RHS) is a function of the magnetic field at the previous time step. The implicit electric field on the left-hand-side (LHS) is a function of the magnetic field at current time step, and relies on $\Delta\vec{B}$. The surface electric field enters in the final term in a surface integral. NIMROD

solves this to update the magnetic field at all points in the domain.

$$\vec{A}_i = \sum_{\nu=R,Z,\phi} \alpha_i e^{in\phi} \hat{e}_\nu \quad (3.1)$$

$$\int_V \vec{A}^* \cdot \Delta \vec{B} dV + \Delta t \int_V \nabla \times \vec{A}^* \cdot \vec{E}_{imp} dV = -\Delta t \int_V \nabla \times \vec{A}^* \cdot \vec{E}_{expl} dV - \Delta t \oint d\vec{S} \times \vec{E}_{surf} \cdot \vec{A}^* \quad (3.2)$$

$$\Delta \vec{B} = \sum_j \Delta B_j \vec{A}_j \quad (3.3)$$

Due to the absence of a zero magnetic divergence condition, as discussed in Section 2.5, a second complementary boundary condition is required to close the system. It is convenient to specify the change in the normal component of the magnetic field separately. During the LHS matrix solve for Eq.(3.2), a homogeneous boundary condition is set for B_{norm} , as it normally is for a perfectly conducting wall to preserve the symmetry of the matrix being solved. After the matrix solve, the normal magnetic field at the wall is updated, consistent with the previously specified electric field in the wall.

In a periodic cylinder, the perturbed fields of interest can be Fourier decomposed both by toroidal mode number n and poloidal mode number m , as in Eq.(3.4).

$$A(r, \theta, z) = \sum_{m,n} A_{m,n}(r) e^{i(m\theta + \frac{nz}{R})} \quad (3.4)$$

This allows the boundary condition to be entirely analytically specified, given the NIMROD perturbed magnetic field at the edge of the domain. NIMROD already performs its calculations with the axial Fourier components, specified by mode number n , so the subroutine calculating the electric field due to the resistive wall need only perform a poloidal Fourier transform for mode number m . The first step in setting the boundary condition is to define the vacuum field outside of the resistive wall and external to the NIMROD domain. For a current-free vacuum region, the magnetic field can be written as the gradient of a scalar potential. For a periodic cylinder, solving Eq.(3.6) gives a scalar

potential that behaves according to a modified Bessel function.

$$\mathbf{B}_{vac} = \nabla\chi \quad (3.5)$$

$$\nabla^2\chi = 0 \quad (3.6)$$

$$\chi = p_1 K_m \left(\frac{nr}{R} \right) e^{i(m\theta + \frac{nz}{R})} \quad (3.7)$$

This external vacuum magnetic field solution can then be matched across a resistive wall with the magnetic fields at the interior of the wall in the NIMROD domain. We make the thin-wall-assumption, in other words, that the wall thickness, δ_w is small compared to the skin-depth of the electric field in the wall and that the normal magnetic field is continuous across the wall.

$$\mathbf{e}_n \cdot [\mathbf{B}_{vac} - \mathbf{B}_{plasma}] = 0 \quad (3.8)$$

$$\mathbf{e}_n \times [\mathbf{B}_{vac} - \mathbf{B}_{plasma}] = \mu_0 \mathbf{K} = \frac{\mu_0 \delta_w}{\eta_w} \mathbf{E}_w \quad (3.9)$$

$$\tau_w = \frac{\mu_0 \delta_w r_w}{\eta_w} \quad (3.10)$$

$$v_w = \frac{\eta_w}{\mu_0 \delta_w} \quad (3.11)$$

While a wall time τ_w is traditionally used to specify the characteristics of the wall and is useful for understanding the time-scale of wall effects, we note that a wall velocity is a more direct characterization, since it doesn't depend on the radial location of the wall, which, in most experiments, varies poloidally. Given the above matching conditions, we can define the (m, n) Fourier components of the electric field in the wall in terms of wall properties, geometry, and the perturbed plasma magnetic fields. We presume that any $n = 0$ components are equal across the wall, so equilibrium quantities can be disregarded. Thus, the (m, n) Fourier component of the electric field in the wall is specified at each time step as:

$$\mathbf{E}^{m,n} = B_{pn}^{m,n} i v_w \frac{K_m \left(\frac{|n|r_w}{R} \right)}{K'_m \left(\frac{|n|r_w}{R} \right)} \left[\frac{n}{R} \mathbf{e}_\theta + \frac{m}{r_w} \mathbf{e}_z \right] + v_w \left[B_{pz}^{m,n} \mathbf{e}_\theta - B_{p\theta}^{m,n} \mathbf{e}_z \right] \quad (3.12)$$

The second boundary condition uses this electric field in Faraday's law to find the change in the normal magnetic field. This change in the normal magnetic field is added to the magnetic field at the edge of the domain and used for calculations in the next time step.

$$\Delta B_n^{m,n} = \Delta t \left(\frac{in}{R} E_\theta^{m,n} - \frac{im}{r_w} E_z^{m,n} \right) \quad (3.13)$$

Finally, all components of the velocity are set to zero at the wall with a traditional no-slip boundary condition.

3.2 Top-hat current profile test case

To verify the periodic cylinder resistive wall boundary condition, we use an analytically simple top-hat current profile equilibrium, for which the RWM growth rate and eigenfunctions have been found by Finn[63]. The equilibrium has a uniform axial magnetic field $B_z(r) = B_0$, equivalent to the toroidal field in a tokamak. The current profile is flat in the plasma and zero in the vacuum region from $r = a$ to $r = r_w$. In the plasma region $r < a$, $q(r) = q_0$. We consider the $\beta = 0$ case. The current and safety factor profiles are shown in Fig 2.

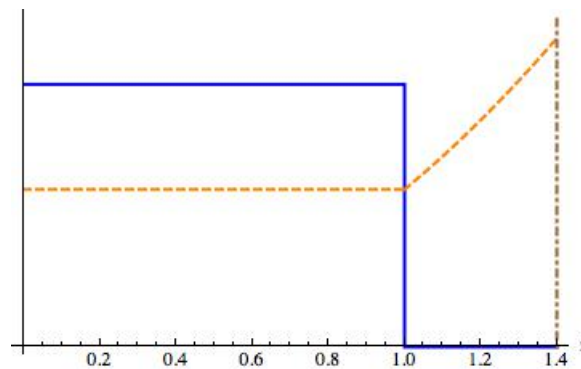


Figure 2: Equilibrium current density profile (in solid blue), q -profile (in dashed orange), and wall location (in dot-dashed brown.)

$$J(r) = J_0 \Theta(a - r) \quad (3.14)$$

$$\rho(r) = \rho_0 \Theta(a - r) \quad (3.15)$$

This equilibrium can be analyzed using reduced ideal MHD, in which derivatives in the axial (z) direction are small. This is a good approximation for a periodic cylinder used to approximate a high-toroidal-field tokamak[64]. The perturbed quantities are proportional to $e^{im\phi + ikz + \gamma t}$. For perturbed magnetic field and velocity $\mathbf{b} = \nabla\psi \times \mathbf{e}_z$ and $\mathbf{v} = \nabla\phi \times \mathbf{e}_z$, the reduced vorticity equation and parallel component of Ohm's law are

$$\gamma \nabla_{\perp} \cdot (\rho \nabla_{\perp} \phi) = \frac{iF(r)}{\mu_0} \nabla_{\perp}^2 \psi - (im/r) J'(r) \psi \quad (3.16)$$

$$\gamma \psi = iF(r) \phi \quad (3.17)$$

where $k = -n/R$, $F(r) = \mathbf{B} \cdot \nabla = (B_{\theta}/r) [m - nq(r)]$, and $\nabla_{\perp} = \nabla - \mathbf{e}_z \partial/\partial z$. Combining these two equations gives an equation for the scalar ψ that represents the perturbed magnetic field.

$$\frac{\mu_0 \gamma^2}{R} \nabla_{\perp} \cdot \left(\rho \nabla_{\perp} \frac{\psi}{F} \right) = -\nabla_{\perp}^2 \psi + \frac{m\mu_0 J'}{rF} \psi \quad (3.18)$$

For a plasma column within a vacuum, surrounded by a perfectly conducting wall at $r_{wall} = c$, we can find the eigenfunction for ψ in the plasma and vacuum regions, using the following equations and matching conditions:

$$[1 + \rho_0 \gamma^2 / F(0)^2] \nabla_{\perp}^2 \psi = 0 \quad r < a \quad (3.19)$$

$$\nabla_{\perp}^2 \psi = 0 \quad r > a$$

$$\lim_{r \rightarrow 0} \psi(r) \rightarrow \infty \quad (3.20)$$

$$\psi(a^+) = \psi(a^-) \quad (3.21)$$

$$\psi'(a^+) - \left(1 + \frac{\mu_0 \rho_0 \gamma^2}{F(0)^2} \right) \psi'(a^-) = -\frac{m\mu_0 J_0}{aF(a)} \psi(a) \quad (3.22)$$

$$\psi(c) = 0 \quad (3.23)$$

In a periodic cylinder with small k , the solutions to the Laplacian in the plasma and vacuum regions are:

$$\psi_{plasma} = \psi_0 r^m \quad (3.24)$$

$$\psi_{vacuum} = \frac{\psi_0}{(1 - (c/a)^{2m})} (r^m - c^{2m} r^{-m}) \quad (3.25)$$

Using these in the condition matching the derivatives of the plasma and vacuum conditions, it is simple to solve for the XK growth rate:

$$\gamma_{xk} = \frac{F(0)^2}{\mu_0 \rho_0} \frac{1}{(1 - (a/c)^{2m})} \frac{J_0 \mu_0}{F(a)} \left(1 - (a/c)^{2m} - \frac{2F(a)}{J_0 \mu_0} \right) \quad (3.26)$$

where the function $F(r)$ is defined as

$$F(r) = \frac{B_\theta(r)}{r} (m - nq(r)) = \frac{B_0}{q(r)R} (m - nq(r)) = \frac{\mu_0 J_0}{2} (m - nq(r)) \quad (3.27)$$

then the final expression for the XK growth rate is:

$$\gamma_{xk}^2 = \frac{2B_0^2}{\mu_0 \rho_0 R^2 q_0^2} \frac{(m - nq_0)}{\left(1 - \left(\frac{a}{c}\right)^{2m}\right)} \left(1 - \left(\frac{a}{c}\right)^{2m} - (m - nq_0) \right) \quad (3.28)$$

Taking the limit as $c \rightarrow \infty$ gives the no-wall XK growth rate.

$$\gamma_\infty^2 = \frac{2B_0^2}{\mu_0 \rho_0 R^2 q_0^2} (m - nq_0) (1 - (m - nq_0)) \quad (3.29)$$

Intermediate to these two cases is the scenario with a wall with some finite resistivity. Equation (3.23) is modified to be a matching condition across a wall of thickness δ_w with resistivity η_w , derived from Ohm's law and Faraday's law:

$$\frac{\delta_w c \mu_0}{\eta_w} \gamma \psi = \left[r \frac{\partial}{\partial r} \psi \right]_{c^-}^{c^+} \quad (3.30)$$

Using this matching condition and a solution ψ_{ext} that is finite as $r \rightarrow \infty$ in the vacuum external to the wall, a dispersion relation for the RWM can be derived. This notation is obtained by identifying the dispersion relations for the XK and no-wall XK modes within

the RWM dispersion relation.

$$\gamma_{RW}^2 = \frac{\gamma_\infty^2 + R(\gamma_{RW})\gamma_{xk}^2}{1 + R(\gamma_{RW})} \quad (3.31)$$

$$R(\gamma) = \frac{1}{2} \left(1 - \left(\frac{a}{r_w} \right)^{2m} \right) \frac{\gamma\tau_w}{m} \quad (3.32)$$

For use in comparing NIMROD results to analytic results, Mathematica was used to solve for γ_{RW} , but by assuming $\gamma_{RW} \ll \gamma_\infty$ (the most common scenario), we can neglect the LHS in Eq.(3.31) and find a simple expression for the RWM growth rate.

$$\gamma_{RW} = \frac{2m}{\tau_w \left(1 - (a/r_w)^{2m} \right)} \left(-\frac{\gamma_\infty^2}{\gamma_{xk}^2} \right) \quad (3.33)$$

For $q_0 = 1.05$ and $a = 1$, the (2, 1) external kink mode is unstable for a perfectly conducting wall at $r_w > 2.115$. It is always unstable in the no-wall limit. For a resistive wall at $r_w < 2.115$, there is an unstable (2,1) RWM. The corresponding eigenfunction for the ideal-wall XK and RWM are (assuming a large major radius, R and plasma-vacuum-interface at $r = 1$),

$$\psi_{xk}(r) = \begin{cases} r^m & r < 1 \\ \frac{1}{(1-c)^{2m}} r^m - \frac{r_w^{2m}}{(1-c)^{2m}} r^{-m} & r > 1 \end{cases} \quad (3.34)$$

$$\psi_{RWM}(r) = \begin{cases} r^m & r < 1 \\ \left(1 - \frac{1}{(m-nq_0)} \right) r^m + \frac{1}{(m-nq_0)} r^{-m} & r > 1 \end{cases} \quad (3.35)$$

While a step-function transition from plasma to perfect vacuum is analytically simple, care must be taken to model it in NIMROD. Since NIMROD uses the MHD equation throughout its domain, the vacuum region between the plasma column and the wall must be modeled as a sparse, highly resistive plasma. The step function in density is smoothed with a transition width w_ρ and is non-zero in the vacuum-like region.

$$\rho = \frac{1}{2} (\rho_{plasma} - \rho'_{vac'}) (\tanh((a-r)w_\rho) + 1) + \rho'_{vac'} \quad (3.36)$$

For these tests the numerical resistivity is a known constant within each grid cell. To model the jump in resistivity between plasma and vacuum, we use a built-in resistivity profile, `tanh-gq`, which finds the cell boundary closest to the location of the plasma vacuum and sets all values of resistivity interior to that point to the plasma resistivity, and all values external to that point to the vacuum-like resistivity. Finally, we use a hyperbolic tangent profile with width w_J for the top-hat current profile, setting J_0 to produce our desired q_0 .

$$J(r) = \frac{1}{2} J_0 (\tanh((a-r)w_J) + 1) \quad (3.37)$$

Because the current profile is not perfectly flat, neither is the q profile in the plasma column. While there are small variations in the toroidal magnetic field and current profiles, the stability is most affected by the mode resonance with the q profile, as defined by the value of q at the axis and at $r = a$. We use Eq.(3.26) along with identifying that $F(a) \propto (m - nq_a)$ and $F(0) \propto (m - nq_0)$ where $q_a = q(r = a)$.

$$\gamma_{xk}^2 \simeq \frac{2B_0^2}{\mu_0 \rho_0 R^2 q_0^2} \frac{(m - nq_0)^2}{\left(1 - \left(\frac{a}{c}\right)^{2m}\right) (m - nq_a)} \left(1 - \left(\frac{a}{c}\right)^{2m} - (m - nq_a)\right) \quad (3.38)$$

Before using this equilibrium to test the resistive wall boundary condition, we must verify that our model adequately represents the analytic equilibrium. There are three major changes being made from the analytic equilibrium and plasma model. First: the plasma simulation has resistivity and viscosity that are necessary to prevent the growth of numerical instabilities, but they must be small enough to reproduce ideal plasma behavior. Second: the region between the current column and the wall is being modeled as a sparse resistive plasma that is governed by the equations of MHD, but it must behave like a vacuum. Third: the transition at the plasma-vacuum-interface (PVI) is smoothed out in the current profile, and the current drop has a finite width. These changes are quantified by the following parameters:

- Electric diffusivity of plasma, η/μ_0

- Kinematic viscosity of plasma and vacuum-like region, ν (does not change at PVI)
- Electric diffusivity of vacuum-like region (measured by Lundquist number, and manipulated by changing the multiplicative factor for the diffusivity profile)
- Ratio of the number density in the vacuum-like region to the number density in the plasma
- Width of tanh current profile, w_J

Parameter scans were performed for a range of wall locations from $r_w = 2.5$ to $r_w = 5$, and the resulting XK growth rates (γ_{nim}) were compared to their analytic counterparts (γ_{calc}). An exact numerical equilibrium would produce $\gamma_{nim}/\gamma_{calc} = 1$. This ratio is plotted for these scans in Fig. 3. The accuracy of the growth rate is improved as the electric diffusivity is decreased and as the viscosity is increased, so the intermediate value of $5m^2/s$ is chosen for both in order to keep $P = 1$. Using an intermediate value of resistivity also allows for a smaller vacuum Lundquist number without a numerically intractable jump in resistivity at the PVI. The best-case equilibrium uses $D_{vac} = 5 \times 10^6$. Similarly, with the vacuum number density and current profile width, values which limit the local gradients are best. The best-case equilibrium uses $N_{vac} = 1 \times 10^{-3}$ and $w_J = 1 \times 10^{-3}$ (though there is no reason that these should be the same value.)

Using this "best-case" equilibrium, a scan of wall location was performed in NIMROD using a perfectly conducting wall. Fig 4 shows the results compared to the analytic curve. The percent error in these cases was within 7%. These cases were not fully converged in spacial resolution or time step, and this may account for the larger error than what is found for the resistive wall cases.

3.3 Verification of NIMROD resistive wall boundary condition for a periodic cylinder

With this equilibrium, the new resistive wall boundary condition can be tested for wall locations $1 < r_w < 2.115$. No RWM would be observed for $r_w \geq 2.115$ because the ideal wall external kink mode would dominate. To estimate the wall parameter, thicknesses between 1 and 5 mm and resistivities between 1×10^7 and $10 \times 10^7 \Omega$ (a standard range for various types of stainless steel) were considered. This gave a range in v_w from $16m/s$ to $800m/s$. This allowed for simulation of a physically realistic resistive wall.

It is possible to allow random numerical noise to initiate the desired instability, but in practice, this can take a prohibitive amount of time. Instead, an instability can be initiated using a small, well-chosen initial perturbation in the magnetic field, velocity, and/or current profiles. For RWM cases, a perturbation in the magnetic field is specified (with corresponding current perturbations for consistency). This is specified using a potential form such that they are divergence-free. The toroidal mode number, n , appears with a negative sign because this equilibrium is unstable to modes with $(m = 2, n = -1)$ helicity. This is equivalent to $(m = -2, n = 1)$ helicity, and since the NIMROD toroidal Fourier components are calculated for positive n , the poloidal Fourier components calculated for the RW boundary condition will be non-zero for $m = -2$.

$$\mathbf{B} = \nabla\psi \times \nabla\zeta \tag{3.39}$$

$$\psi = \psi_0 \psi(r) \cos(m\theta - n\phi) \tag{3.40}$$

Instead of using the expected eigenfunction of the RWM (which would not provide a good test of the simulation's ability to reproduce these profiles), we use a different ψ profile, but one that still has a discontinuous slope at the plasma vacuum interface and a non-zero

value at the wall.

$$\psi(r) = \begin{cases} r^m & r < 1 \\ \left(1 + \frac{1}{(m-nq_0)}\right)r^m - \frac{1}{(m-nq_0)}r^{-m} & r > 1 \end{cases} \quad (3.41)$$

This is equivalent to having a non-zero value of the normal magnetic field at the wall, which seems to be critical for quickly observing a growing RWM. This perturbation leads to a larger-than-desired value of $\nabla \cdot \mathbf{B}$ during the first few time steps, but this returns to an acceptably small value as the perturbed profiles shift to the RWM eigenfunction. Fig 5 shows the analytic solution and NIMROD result for the $B_{norm}^{n,m}$ eigenfunction with the wall at $r = 1.4$. It should be noted that the ratio of $B_{norm}(r_w)$ to $B_{norm}(1)$ becomes smaller as the wall location is increased, until $B_{norm}(r_w) = 0$ at the ideal-wall stability limit of $r_w = 2.115$, showing the smooth transition from RWM to XK for this equilibrium.

Studies were done varying the wall parameter v_{wall} and the wall location, r_{wall} in NIMROD. They produced growth rates that matched the analytic solution to within 1%. These are shown in Fig 6.

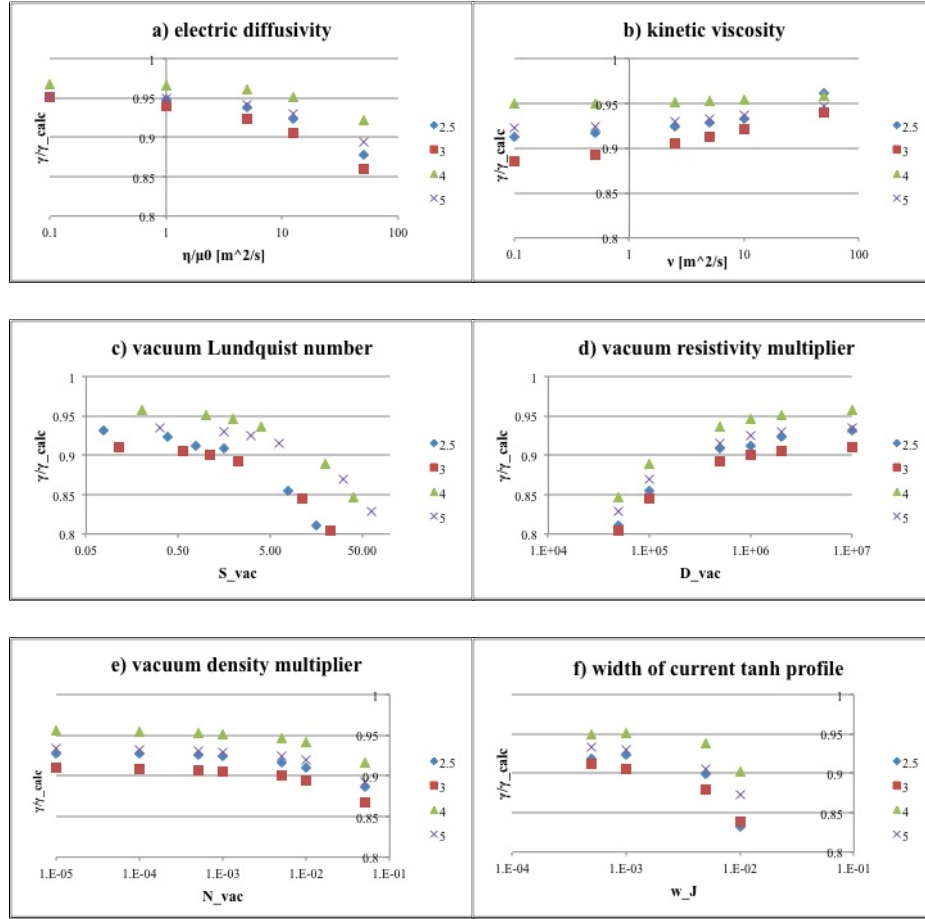


Figure 3: NIMROD growth rates normalized to the analytic growth rate for scans of a) plasma electric diffusivity η/μ_0 in [m^2/s] with vacuum multiplier varied to keep S_{vac} constant, b) kinematic viscosity ν in [m^2/s], c) vacuum Lundquist number S_{vac} and the parameter used to adjust it in NIMROD, d) the vacuum resistivity multiplier D_{vac} where $\eta_{vac} = D_{vac}\eta_{plasma}$, e) the vacuum density multiplier N_{vac} where $n_{vac} = N_{vac}n_{plasma}$, and f) the width of the tanh current profile, with logarithmic x-axes. Different radii are shown by $r = 2.5$:blue diamonds, 3:red squares, 4:green triangles, 5: purple crosses

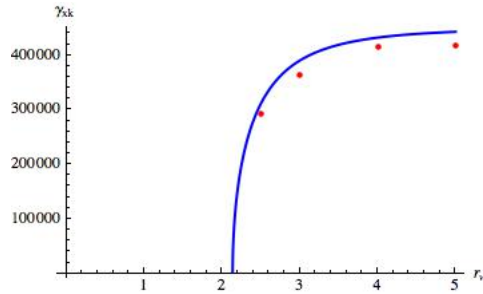
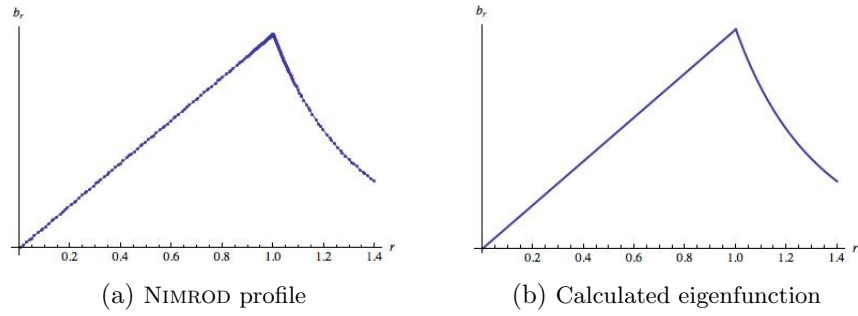
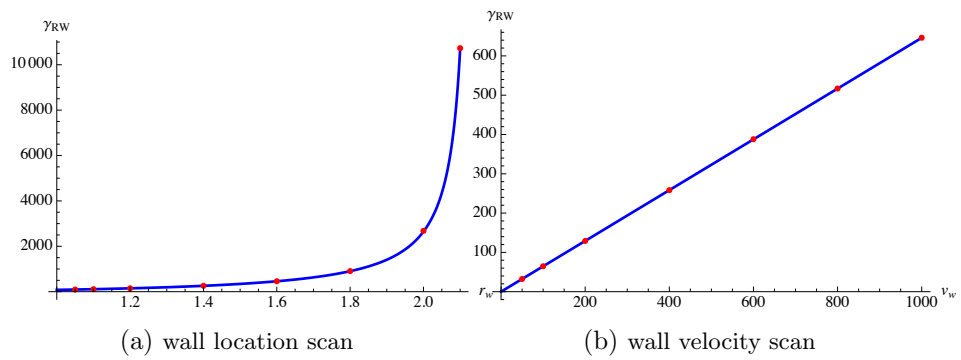


Figure 4: Calculated external kink growth rates in blue and NIMROD results as red dots. The calculated growth rate for a wall at ∞ is 4.5×10^5 , and one can see how this is approached as the wall is moved outward.

Figure 5: NIMROD and calculated B_{norm} profilesFigure 6: Calculated RWM growth rates in blue (dashed orange shows growth rates without q_a correction) and NIMROD results as red dots

Chapter 4

External error fields in a periodic cylinder

With a NIMROD boundary condition that correctly handles non-zero normal magnetic field at the wall, it is natural to extend it to include an externally imposed normal magnetic field. When the perturbed fields are resonant with a magnetic surface, they can be used to drive islands in otherwise stable equilibria. Non-resonant fields can drive an ideal displacement of the plasma. NIMROD can be used to study mode-locking and other inherently non-linear interactions between the error field and the plasma.

4.1 Implementation in NIMROD

Instead of imposing a constant normal magnetic field at the wall, as is often done in error-field theory, here the system is modeled as a helically perturbed current sheet at some location outside of the wall that creates a perturbed magnetic field that penetrates the resistive wall at a time scale dependent on wall properties. As is done for the resistive wall on its own, we solve for the scalar potential of the vacuum magnetic field, but now with an additional domain boundary outside the wall, across which the solutions must be appropriately matched. Vacuum region 1 is defined as $r_w < r < r_{EF}$ and vacuum region

2 is defined as $r > r_{EF}$.

$$\mathbf{B}_{vac} = \nabla\chi \quad (4.1)$$

$$\nabla^2\chi = 0 \quad (4.2)$$

$$\chi_1 = \left[p_1 K_m \left(\frac{nr}{R} \right) + p_2 I_m \left(\frac{nr}{R} \right) \right] e^{i(m\theta + \frac{nz}{R})} \quad (4.3)$$

$$\chi_2 = p_3 K_m \left(\frac{nr}{R} \right) e^{i(m\theta + \frac{nz}{R})} \quad (4.4)$$

$$\mathbf{e}_n \cdot [\mathbf{B}_{outer} - \mathbf{B}_{inner}] = 0 \quad (4.5)$$

$$\mathbf{e}_n \times [\mathbf{B}_{v1} - \mathbf{B}_{plasma}] = \mu_0 \mathbf{K} = \frac{\mu_0 \delta_w}{\eta_w} \mathbf{E}_w \quad (4.6)$$

$$\mathbf{e}_n \times [\mathbf{B}_{v2} - \mathbf{B}_{v1}] = \mu_0 \mathbf{K}^{EF} \quad (4.7)$$

For a resonant, helical surface current, the poloidal and toroidal components of the surface current must be related by

$$K_\theta = \frac{-nr_{EF}}{mR} K_\phi \quad (4.8)$$

Thus, the effective magnitude of the applied B_{norm} perturbation at the wall is set by the toroidal helical current and geometrical factors. To determine the resulting B_{norm} for comparison to studies in which the $B_{norm}(r_w)$ is explicitly stated, NIMROD was run with a non-resonant equilibrium (usually one of the opposite helicity) and the error field penetrated the plasma until it reached a constant value at the wall.

From these matching conditions, we can derive the electric field at the wall.

$$\mathbf{E}^{m,n} = v_w \left[iC B_{pn}^{m,n} \left(\frac{n}{R} \mathbf{e}_\theta + \frac{m}{r_w} \mathbf{e}_z \right) + \left(B_{pz}^{m,n} \mathbf{e}_\theta - B_{p\theta}^{m,n} \mathbf{e}_z \right) - \mu_0 G_{EF} K_\phi^{EF} \left(\frac{r_{EF} n}{mR} \mathbf{e}_\theta + \frac{r_{EF}}{r_w} \mathbf{e}_z \right) \right] \quad (4.9)$$

$$C = \frac{K_m \left(\frac{|n|r_w}{R} \right)}{K'_m \left(\frac{|n|r_w}{R} \right)} \quad (4.10)$$

$$G_{EF} = \frac{K_m \left(\frac{|n|r_w}{R} \right) \frac{I_m \left(\frac{|n|r_w}{R} \right)}{K'_m \left(\frac{|n|r_w}{R} \right)} - I_m \left(\frac{|n|r_w}{R} \right)}{K_m \left(\frac{|n|r_{EF}}{R} \right) \left[1 - \frac{I_m \left(\frac{|n|r_{EF}}{R} \right)}{K'_m \left(\frac{|n|r_{EF}}{R} \right)} \right]} \quad (4.11)$$

The first two sets of parentheses are simply the RW boundary condition. The final term is the effect of the external error field. The second boundary condition, which specifies the change in B_{norm} , is the same as Eq.(3.13).

4.2 Equilibrium for testing error-field driven islands in NIM-ROD

To study error-field-driven islands and their behavior, a tearing- (and kink-) stable equilibrium with small m/n rational surface, such as $q=2, 3$, or 4 is needed. The stability is determined by applying an error-field to the equilibrium with no flow and measuring the amplification of the error-field by the plasma at the resonant surface once it is fully saturated. If the mode keeps growing and doesn't reach a saturated state, it is unstable. If it saturates, the stability parameter is defined as

$$-\Delta' = 2m \frac{\mathbf{e}_n \cdot \mathbf{B}_{vac}(r_s)}{\mathbf{e}_n \cdot \mathbf{B}_{pla}(r_s)} \quad (4.12)$$

The set of profiles described by Furth, Rutherford, and Selberg includes configurations that are stable, given that there is no pressure[65]. They were also already included in the NIMROD code for use in regression testing. For a specified q_0 , r_0 , and λ , the profiles are defined as

$$q = q_0 \left[1 + \left(\frac{r}{r_0} \right)^{2\lambda} \right]^{\frac{1}{\lambda}} \quad (4.13)$$

The most stable equilibrium with a $q = 2$ surface is near marginal stability, so we consider equilibria with a $q = 3$ surface and with a $q = 4$ surface. These equilibria are shown in Fig. 7 and their defining parameters are shown in Table 1.

This equilibrium has no vacuum-like region built into the current profile. When the plasma region extends all the way to the wall, it responds to the RW boundary condition

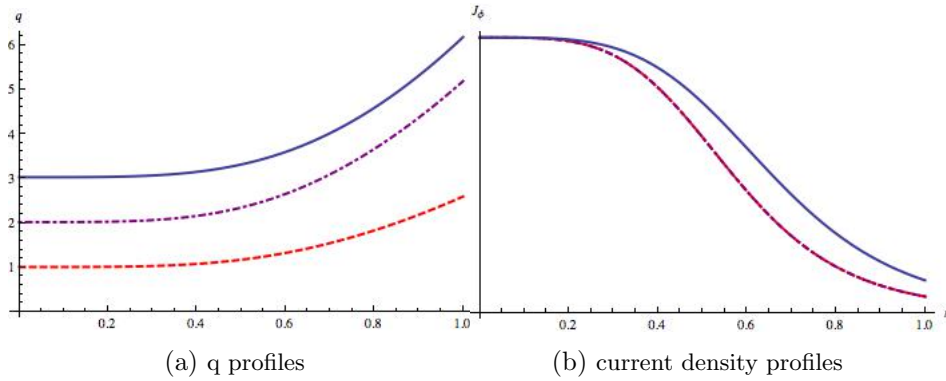


Figure 7: Profiles of q and current density for stable $q = 4$ resonant (solid blue), $q = 3$ resonant (dot-dashed purple) and marginally stable (dashed red) Furth-Rutherford-Selberg profiles. In (b) the lower two profiles are the same and appear as one line.

	q_0	r_0	λ	$(-\Delta')$
$q = 4$ resonant	3.03	0.75	2	2.24
$q = 3$ resonant	2.02	0.65	2	0.2
marginally stable	1.01	0.65	2	≤ 0

Table 1: Furth-Rutherford-Selberg profile parameters considered for error field studies with associated stability parameters.

by creating an unphysical boundary layer. To eliminate this, we include a small vacuum-like region using a tanh-function profile that decreases density and a step-function that increases electrical diffusivity at a location far from the rational surface, and close to the wall ($r = 0.95$).

To compare our results with the predictions of Fitzpatrick[4], plasma and geometry parameters are chosen to best meet the requirements of the visco-resistive regime. For runs which require axial rotation, a constant equilibrium velocity profile, $V_z(r) = V_0$, is used. This does not affect the other equilibrium quantities.

There was some difficulty in choosing a good parameter regime to study. In general, the Furth-Rutherford-Selberg profiles do not have a large enough stable parameter space to allow the necessary adjustments to find a good equilibrium that is both numerically feasible and within the linear, constant- ψ regime during a bifurcating mode-locking event. As equilibrium profiles, resistivity, viscosity, and density were varied, all stable cases led

to a critical rotation (calculated by Eq.(2.3.3)) that required a large error field to lock it to the wall - so large that the resulting island width was larger than the linear layer width. Thus, the driven island locking studies are performed in a regime where non-linear island physics is most likely at play. Nonetheless, the locking of a driven island to the wall in a rotating plasma is successfully demonstrated with NIMROD.

4.3 Linear simulation results from error field studies

The stable $q = 4$ resonant profile was used with the following equilibrium parameters: $R_0 = 5$, $B_0 = 1$, $n_0 = 2.4 \times 10^{21}$, $S = 3 \times 10^6$, and $P = 1$. The layer time associated with a resonant surface in these equilibria can be calculated using Eq.(2.35). For comparison, I also calculated it from the poloidal shift of the maximum amplified error field at the rational surface, using the previously measured Δ' and fitting to

$$\sin(m\Delta\theta) = \frac{\omega\tau_{L^*}}{\sqrt{1 + (\omega\tau_{L^*})^2}} \quad (4.14)$$

$$\tau_{L^*} = \frac{\tau_L}{-\Delta'} \quad (4.15)$$

For all stable equilibria for which this was done, the calculated and measured layer times agreed to within almost a factor of 2. For this equilibrium, the calculated layer time was $8.8 \times 10^{-2}s$ and the measured layer time was $4.2 \times 10^{-2}s$. However, both these methods assume linear layer physics.

A series of runs was performed using only terms from the linearized MHD equations. With only this physics included, the shielding of error fields by rotation is present, but the error field cannot slow the plasma via an electromagnetic torque or lock to the wall. Refer to Sections 2.3.2 and 2.3.3 for the theory related to this. When a vacuum or non-resonant equilibrium is present, the error field drops off once it is past the wall, as seen in Fig. 8a. When a resonant equilibrium is present, the error field is amplified at the resonant surface,

which is at $r = 0.7$ for this case. Finally as a larger and larger equilibrium flow is added, the plasma interior to the resonant surface is shielded from the error field by a sustained current sheet at the rational surface - these profiles are seen in Fig. 8.

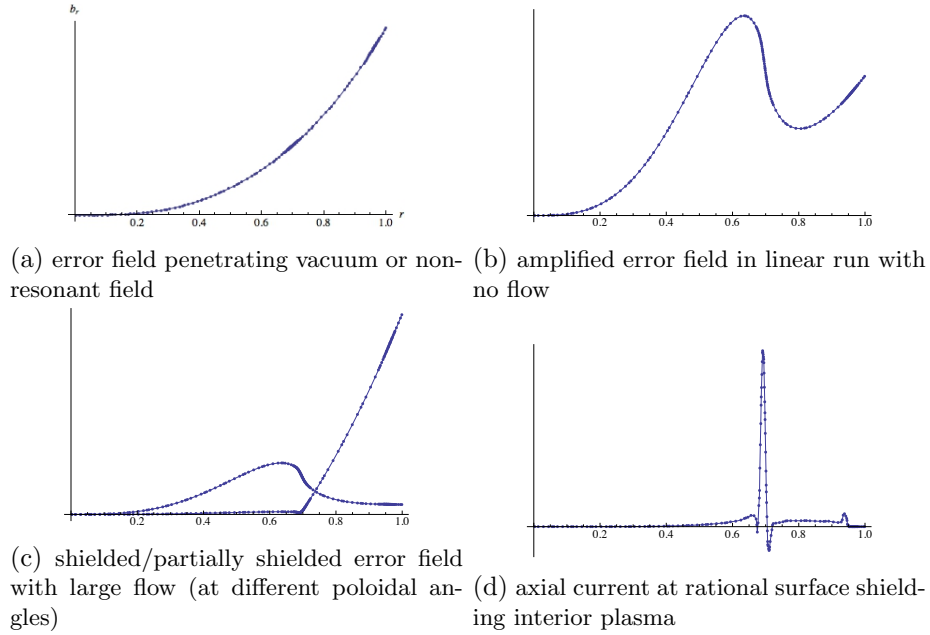


Figure 8: Linear results from NIMROD from (a) a non-resonant case, (b) a case without flow, and (c) and (d) a case with large flow, all with an error-field of the order of the critical locking value for the flow velocity.

The effect of plasma shielding by rotation can also be seen in Poincaré plots of the cross-section. A case with no flow is shown in Fig. 9. In this case, islands are in phase with the helical applied error field. Fig. 10 shows a case with large flow. Not only are island widths reduced in the case with equilibrium flow, but the remaining islands are shifted out of phase from the applied error field, according to Eq.(4.15). This helps explain the strange shapes of the profiles in Fig. 8c: as the flow shields the plasma from the error fields, it is also pulling the mode out of phase from its source. However, one can see that the reduced island widths are still a significant fraction of the 1m minor radius, while the calculated linear layer width is only 5mm. Thus it is clear that the island width exceeds the layer width, and linear layer theory will not be valid when we proceed to demonstrate

mode-locking. Instead, this most likely falls in the nonlinear Rutherford layer regime[28].

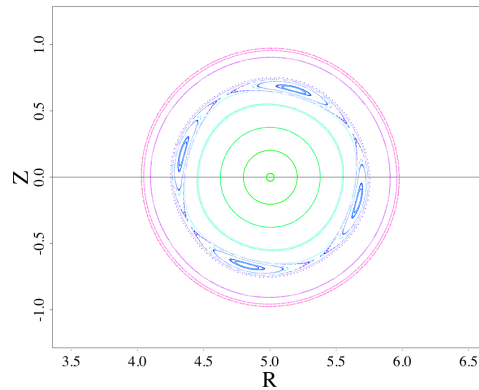


Figure 9: Poincaré plot of linear case with penetrating resonant error field and no flow.

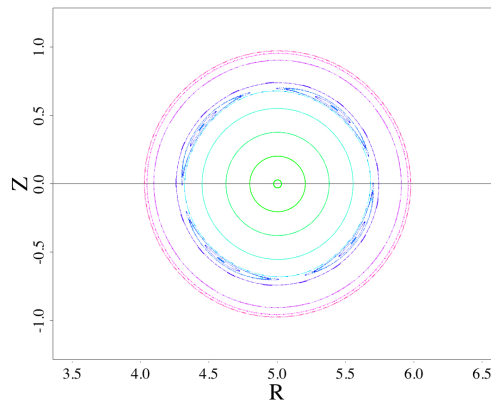


Figure 10: Poincaré plot of linear case with resonant error field and large flow.

4.4 Nonlinear simulation results from error field studies

Including nonlinear terms in the NIMROD simulation allows for mode-locking to be observed. These runs use toroidal mode numbers $n = 0, 1$, and 2. When there is no equilibrium rotation, the results are the same as in the linear runs. However, when rotation is included in the equilibrium, a sufficiently large error-field can penetrate the flowing plasma and reduce $\mathbf{k} \cdot \mathbf{V}$ to zero at the rational surface, essentially locking the plasma to the wall. The resulting islands are in the same poloidal phase as they would be with no flow, and

have the same width. In Fig. 11 is the penetrating amplified error field in a case with large equilibrium flow, and in Fig. 12 is the Poincaré plot of the large islands, unaffected by the equilibrium flow.

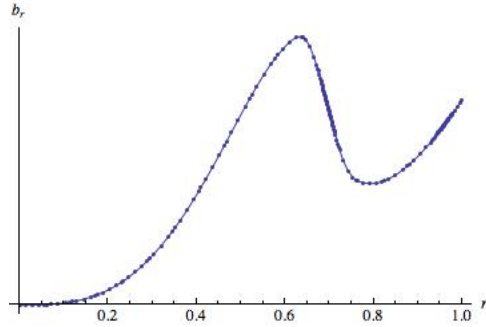


Figure 11: Radial magnetic field showing the penetration and amplification of the error field despite the large equilibrium flow.

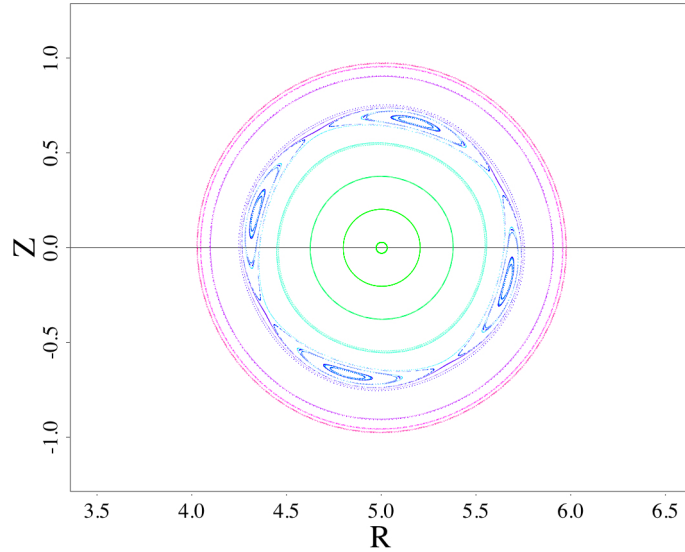


Figure 12: Poincaré plot of non-linear case with resonant error field and large flow.

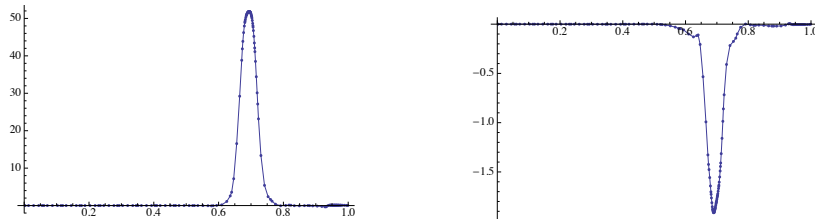
Because there is no poloidal flow damping included in this model, a perturbed poloidal flow at the rational surface is the major factor in reducing $\mathbf{k} \cdot \mathbf{V}$ to zero there. The positive perturbed poloidal flow and the negative perturbed toroidal flow are shown in Fig. 13. One can derive a poloidal torque balance equation equivalent to that derived in Section 2.3.3. Together, these give an equation that includes both toroidal and poloidal flow. The

critical rotation at which bifurcation occurs is the same as when there is only toroidal flow, but the critical locking error field is modified.

$$\omega = \mathbf{k} \cdot \mathbf{V} = \frac{m}{r_s} V_\theta - \frac{n}{R_0} V_\phi \quad (4.16)$$

$$\left(\frac{m^2}{r_s^2} + \frac{n^2}{R_0^2} \right) \frac{2m^2 \tau_s \left(\int_{r_s}^{r_w} dr / (r \rho \nu) \right) |\Psi_v|^2}{\mu_0 (-\Delta')^2} \frac{\omega}{(1 + (\omega \tau_s / (-\Delta'))^2)} = \omega_0 - \omega \quad (4.17)$$

$$|\Psi_v|_{lock} = \frac{m \omega_0}{2r_s^2} \sqrt{\left(\frac{m^2}{r_s^2} + \frac{n^2}{R_0^2} \right)^{-1} \frac{\mu_0 \tau_s}{2 \left(\int_{r_s}^{r_w} dr / r \rho \nu \right)}} \quad (4.18)$$



(a) perturbed poloidal flow at the rational surface (b) perturbed toroidal flow at the rational surface

Figure 13: The $n = 0$ velocities driven at the rational surface in a non-linear run with an applied error field and a toroidal flow.

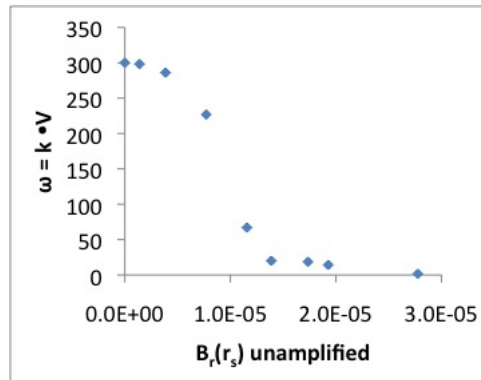


Figure 14: Net rotation plotted versus a measure of the error field amplitude (in this case, the error-field amplitude at the rational surface in a vacuum.)

Both the linear and nonlinear studies use an equilibrium toroidal flow of 1500 m/s, which is above the critical value for bifurcation predicted by linear layer physics, which is 1390 m/s. However, this flow is not necessarily large enough to account for the non-linear

nature of the large islands required to lock the flow in such a stable equilibrium. Thus, the plot of $\mathbf{k} \cdot \mathbf{V}$ against the error-field magnitude in Fig. 14 does not show the abrupt jump that would signify a bifurcated state, but it does eventually reach a point where the mode is locked to the helicity of the error field and not rotating with the plasma.

Chapter 5

General resistive wall boundary condition

Modeling the resistive wall for a toroidal geometry and a non-circular plasma cross-section requires that poloidal mode numbers be coupled, instead of separated out into poloidal Fourier components. The resulting boundary condition can be used not only for a torus, but also for a periodic cylinder - thus we refer to it as a general boundary condition. The previous resistive wall studies in a periodic cylinder are used for comparison throughout code development and for final verification.

5.1 Implementation in NIMROD

5.1.1 Natural boundary condition on the electric field

In a generalized geometry, the same jump conditions across the resistive wall are used, but the way in which the external magnetic field is found is different. B_{vac} is still defined as the gradient of a scalar, but the solution for the scalar is no longer simple Bessel functions. Now it is defined as

$$\mathbf{B}_v = \nabla\chi \tag{5.1}$$

$$\chi = \chi_n e^{in\phi} \tag{5.2}$$

$$\chi_n(w) = \sum_{w'} M_n(w, w') B_{norm}^n(w') \tag{5.3}$$

where w and w' are the locations of all points on the boundary and M_n is the vacuum response matrix for a toroidal Fourier number n . M_n is found by the external vacuum solver, GRIN[52] for toroidal geometries, or determined analytically for a periodic cylinder. The process for finding M_n for the periodic cylinder is included in Appendix A, and the subtleties of interfacing with GRIN are discussed in Section 5.1.3. M_n is loaded into the appropriate arrays only once at the beginning of a run. It is not time dependent. The boundary condition on the electric field then is

$$\mathbf{E}^n = v_w \left[\left(\frac{-in}{R} \chi + B_{p\phi} \right) \mathbf{e}_\theta + (\nabla_\theta \chi - B_{p\theta}) \mathbf{e}_\phi \right] \quad (5.4)$$

where θ denotes the direction tangential to the surface in the R-Z plane, not the poloidal angle in cylindrical coordinates.

5.1.2 Dirichlet boundary condition on the normal magnetic field

We specify a dirichlet boundary condition for the normal magnetic field as an additional boundary condition. We avoid taking additional derivatives of the electric field and instead multiply Faraday's law by test functions α_i and integrate over the wall surface to create a weak-form surface integral that only requires known derivatives of the test functions. These test functions are the same as the basis functions used to represent the field at nodes within each computational element. The full derivation of this is included in Appendix B. This condition is only valid for sufficiently smooth walls, where a value of the normal vector can be determined at element boundaries.

$$\sum_q \hat{n} \cdot \Delta \mathbf{B}_q \int_S \alpha_p \alpha_q dS = \Delta t \int_S \left[\hat{\phi} \cdot \mathbf{E} \frac{1}{h_\tau} \frac{d\alpha_p}{d\tau} + \frac{in\alpha_p}{R} \hat{\theta} \cdot \mathbf{E} \right] dS \quad (5.5)$$

Here, τ is the poloidal grid coordinate and h_τ is the scale factor $|\partial \mathbf{r} / \partial \tau|$. If we choose Gauss-Lobatto-Legendre (GLL) spacing for the nodes within the cell and a Lobatto integration scheme for the edge, the inversion of the LHS of Eq.(5.5) becomes much simpler,

because

$$\int_S \alpha_p \alpha_q (x_{GLL}) dx = \delta_{pq} w_p \quad (5.6)$$

where w_p is the integration weight of the test function. Because GLL nodes include cell vertices that lie on block boundaries, the calculation is not entirely local for parallel runs, but information can be quickly seamed at block borders using machinery already in place in NIMROD.

5.1.3 Interpolation with GRIN

The GRIN code uses a Green's function approach for a variety of elliptic operators, including Laplace and Grad-Shafranov. After NIMROD preprocessing produces the grid for a given run, GRIN is run to find the matrix $M_n(w, w')$. This only needs to be calculated once for a given computational grid. GRIN inverts the normal component of Equation (5.1). At every time step the matrix multiplication in Equation (5.3) must be performed for each toroidal mode number. This couples information poloidally along the full wall and is therefore a global calculation. It has been implemented such that a global $\hat{n} \cdot \mathbf{B}_n$ is communicated to each processor, which uses a subsection of rows of the M_n matrix to compute the local χ_n .

A major complication to this implementation is transforming between the different NIMROD and GRIN basis functions. The GRIN code uses piecewise-constant zonal-basis functions, whereas NIMROD has high-order spectral elements with GLL node spacing. Empirical tests show that GRIN is not accurate when the zonal-basis functions are simply placed between the non-uniform GLL nodes. Improved performance is obtained when a number of GRIN zonal-basis functions are evenly spaced within each element such that the GRIN and NIMROD edge degrees of freedom remain equal.

In order to find χ_n using M_n produced by GRIN, the normal component of the perturbed

magnetic field is first converted to the GRIN basis using a simple average of uniformly-spaced evaluations of the NIMROD basis-functions with a GRIN zone. The matrix multiplication is then performed at the GRIN nodes. The final interpolation back into the NIMROD basis is more complicated. Simply projecting into the NIMROD basis from GRIN's piecewise constant basis functions produces significant error. Two interpolation methods were implemented. The first uses a uniformly weighted average to set the values directly at the GLL nodes. The second uses global cubic spline evaluations of the χ_n values at the GRIN nodes. Relative to the average method, the spline method is more computationally expensive in that it requires additional global communication among processors that own the boundary degrees of freedom. Initial convergence scans (as discussed in Section 5.3) showed particularly poor performance using the average method, so only the spline method was pursued.

Development of this code included the revision of the cylindrical RW boundary condition to allow non-uniform point spacing, and the ability to specify different integration schemes for the interior bulk region and the edge.

5.2 Resistive wall boundary condition verification

5.2.1 Verification in a periodic cylinder

Initial testing of the general RW boundary condition uses the equilibrium and run parameters covered in Section 3.2. This makes use of the analytic vacuum response matrix M_n calculated and used at the NIMROD node locations. As seen in Fig. 15, the RWM growth rates using the generalized boundary condition match the analytic growth rates to within 3% as the wall location is varied. Fig. 16 compares magnetic field and velocity profiles from cases run with the periodic cylinder boundary condition with cases run with the generalized boundary condition.

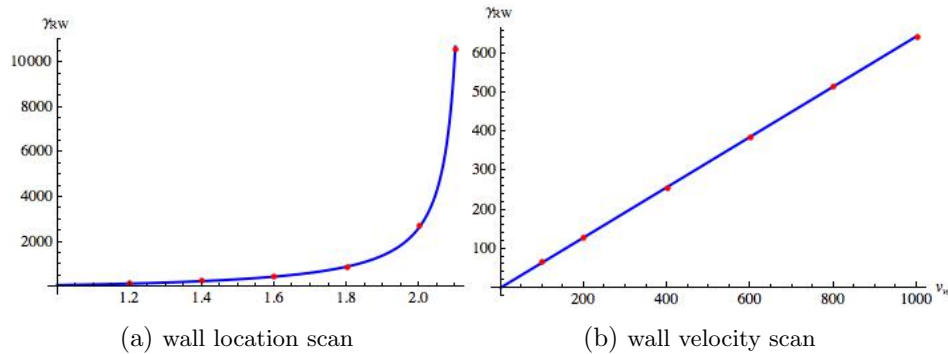


Figure 15: Calculated RWM growth rates in blue and NIMROD results as red dots

The good agreement with the previous analytic and numerical work for the cylindrical case in growth rates and profiles verifies that the formulations for the electric field in the wall and the change in the normal magnetic field are correct.

5.2.2 Verification in a large-aspect-ratio torus

As the general resistive wall boundary condition was refined, it was tested for a torus with a circular poloidal cross-section. This test used an earlier version of the boundary condition that used a vacuum response matrix M_n calculated by GRIN at the NIMROD GLL nodes without interpolation between bases. Because there were no exact analytic results to compare against, it was merely used to determine whether GRIN and the NIMROD machinery for reading the GRIN matrix were successfully capturing the poloidal mode coupling introduced by toroidal geometry. A hyperbolic tangent current profile similar to that used for previous benchmarks (see Section 3.2) was input into NIMROD's Grad-Shafranov solver, NIMEQ, to create a toroidal equilibrium unstable to the RWM.

$$J(\psi) = \frac{1}{2} J_0 (\tanh((\psi_v - \psi) w_J) + 1) \quad (5.7)$$

Here, ψ_v is adjusted to be the value of ψ at $r = 1$. The magnitude of the current profile, J_0 is chosen for a given aspect ratio such that $q_0 = 1.05$, and the minor radius is kept fixed at $r_w = 1.4$. The RWM eigenfunction and growth rate were predicted to approach

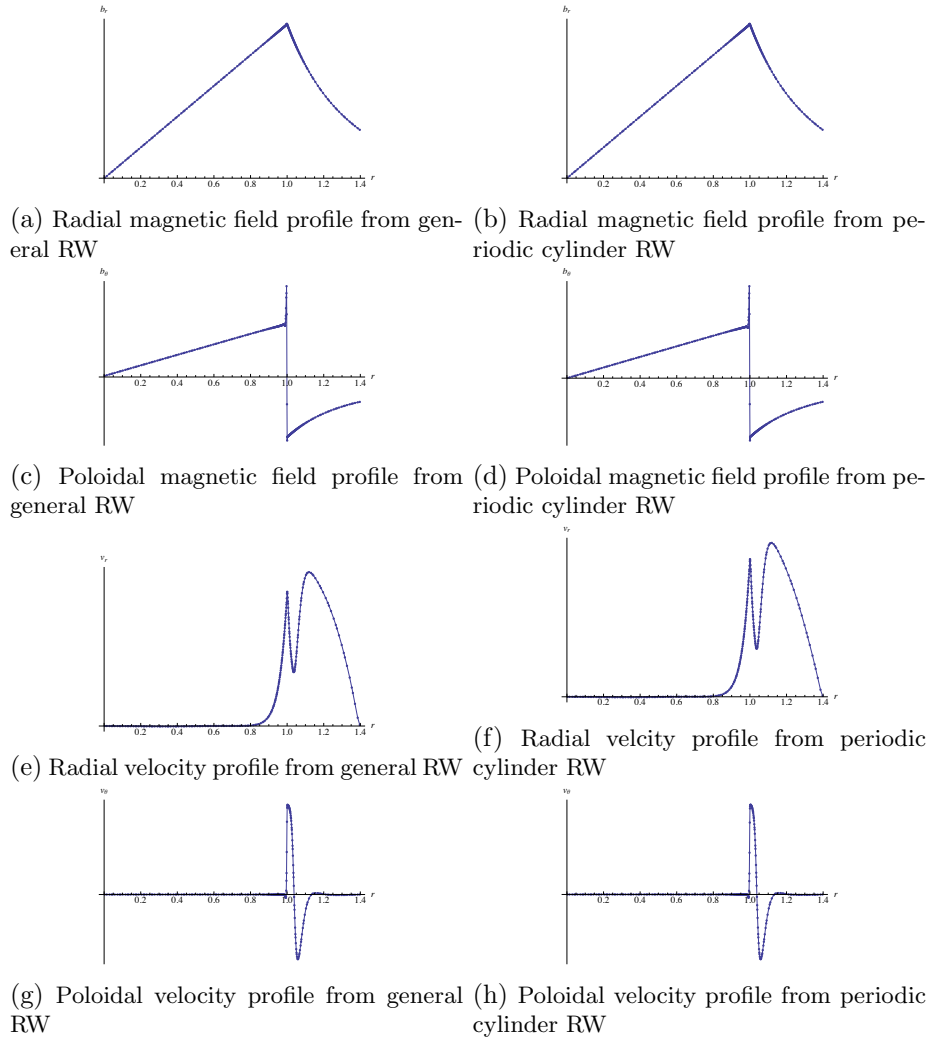


Figure 16: Comparison of magnetic field and velocity profiles from generalized and periodic cylinder resistive wall boundary conditions

the analytic results predicted for a periodic cylinder as the aspect ratio is increased. The results from the aspect ratio scan are shown in Fig. 17. The growth rate eigenvalue of the system is sensitive to q at the edge as it varies slightly with major radius. Different decompositions of poloidal mode number m are coupled together at different aspect ratios, causing the small non-monotonic variation.

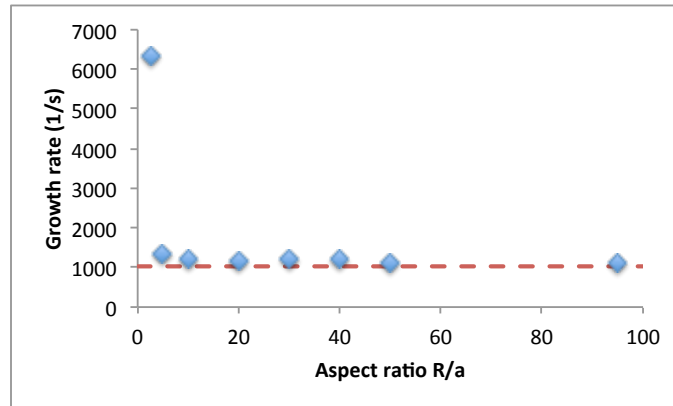


Figure 17: RWM growth rate in a circular-cross-section torus versus aspect ratio (blue dots) converging on the value of the RWM growth rate in a periodic cylinder (dashed red line)

5.3 Spatial convergence studies

In order to rigorously test the performance of the resistive wall boundary condition, spatial convergence studies were performed for a variety of geometries. For calculations performed using the spectral element method, one can examine the convergence properties as the element spacing is decreasing (and the number of elements is increased), called h-refinement, or as the number of polynomial degrees within each element is increased, called p-refinement. For h-refinement, an optimal spectral element code is expected to achieve algebraic convergence with a rate of $(p + 1)$ [66]. For p-refinement, geometric convergence is expected.

5.3.1 Convergence for a large aspect ratio torus

Convergence scans were performed for a circular cross-section torus with major radius $R = 50$, plasma minor radius $a = 1$ and resistive wall minor radius $r_w = 1.4$. The equilibrium from Section 5.2.2 was modified by increasing the width of the hyperbolic tangent current profile. This was done so that resolution at the sharp drop in equilibrium current would not limit convergence even at low polynomial degree. As was seen in Figure

17, there is some variation in growth rate even at very large aspect ratio. Because of this, and the broadening of the current profile, it is not practical to use the analytic growth rate derived in Section 3.2 to calculate error. Instead, we tried two different approaches: either running the case with large polynomial degree and a large number of poloidal cells and using the resulting growth rate as a point of comparison, or, in later scans, assuming algebraic convergence as we varied the number of elements and choosing the 'correct' growth rate, γ_0 , that gave a best fit in order to find the rate of convergence.

The first convergence scan studies were performed using the averaging method for interpolating between NIMROD and GRIN. These also used a high resolution run to determine a growth rate to calculate error from. The h-refinement results, seen in Fig. 18, demonstrated that there were some major issues to be resolved. The convergence rates for odd polynomial degrees (3 and 5) were of the same order and less than 3, while they should have been approximately 4 and 6, respectively. Additionally, this method of finding the so-called correct growth rate underestimates the error, so the actual convergence rate is worse than calculated here. The other problem apparent in these results is that the even polynomial degrees (4 and 6) show no convergence: the percent error remains large and essentially the same as the number of elements is increased. This pointed to a possible problem with the interpolation scheme, and alternative methods were explored, as presented in Section 5.1.3. The spline method for interpolation produced promising results in preliminary testing, so h-refinement scans were done to more quantitatively measure its performance. Knowing that large errors were possible even at high resolution, a growth rate for comparison was determined by finding the best fit of the data to a power equation. The results for polynomial degrees 3 and 4 are shown in Fig. 19. Even polynomial degrees now behave similarly to odd ones, but the convergence rates for both are too small, with rates < 2 . The reduced convergence rate is most likely because the comparison growth rate was found using the best-fit method instead of a high-resolution run.

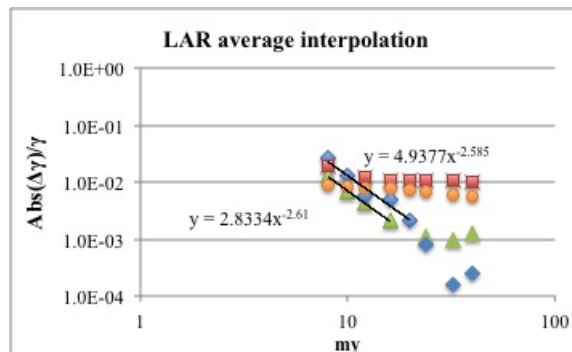


Figure 18: Error in growth rate compared to high resolution case when using average interpolation scheme. (pd=3 in blue diamonds, pd=4 in red squares, pd=5 in green triangles, pd=6 in orange circles)

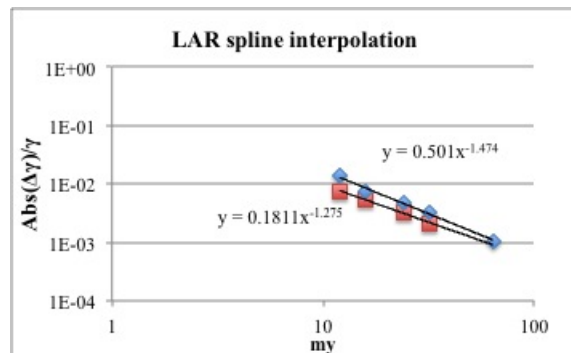


Figure 19: Error in growth rate compared to best fit γ_0 using spline interpolation scheme. (pd=3 in blue diamonds, pd=4 in red squares)

5.3.2 Convergence for a periodic cylinder

Because of the relative simplicity of the periodic cylinder geometry, there were a number of ways to narrow down the source of the poor convergence properties observed for the large aspect ratio torus. The second method for finding a γ_0 was used for these tests. In these cases, there was very little difference between rates of different polynomial degrees, and so only one is reported here, either 3 or 4. The h-convergence rates for the base case and for various modifications are listed in Table 2.

Based on the convergence results for the large aspect ratio torus, it was known that spline interpolation from GRIN to NIMROD performed better than an averaging interpolation. For the periodic cylinder, since the analytic vacuum response matrix is calculated

by NIMROD, we could simply calculate it at the NIMROD GLL nodes, in order to see if the spline interpolation was the source of the poor convergence. However, the rate of convergence without any interpolation to find χ was still approximately 1. In order to simplify the interpretation of any other periodic cylinder results, the matrix calculated at the GLL nodes was used for the rest of the periodic cylinder convergence studies (unless otherwise noted.)

Another adjustment was to change the orientation of the cylinder with respect to the grid. Instead of a polar grid with the linear periodic length of the cylinder in the Fourier direction, a rectangular grid was used with toroidal (instead of linear) geometry in the Fourier direction. Figure 20 shows how these two numerical grids relate to the periodic cylinder geometry. This change required minimal adjustments to the resistive wall boundary condition code, primarily redefining the size of the system in the Fourier direction; the bulk of the physics derivation was still applicable for this new geometry. The advantage of changing to a rectangular mesh was that the normal vector at the wall is the same at all points along the numerical domain. An improvement in convergence using this grid would indicate that error was being introduced by neglecting the derivative of the normal unit vector in the derivation leading to Equation 5.5. However, the rate of algebraic convergence when increasing the number of cells remained near 1. This indicated that our assumption that the normal unit vector did not change significantly from one cell to another was not the primary source of error leading to slow convergence.

Another test took advantage of the analytic resistive wall boundary conditions described in Section 3.1. By modifying the electromagnetic boundary condition management routine, the surface electric field could be calculated using the original analytic method, while the change in the normal magnetic field was still calculated using the new general geometry method. The algebraic h-convergence rate using this modification was much improved at 3.34, with smaller percent errors. This indicated that the source of the error

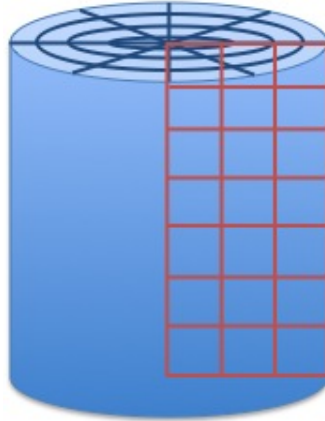


Figure 20: Polar grid in blue and rectangular grid in red superimposed on a periodic cylinder

was in the calculation of the surface electric field, and that the normal magnetic field boundary condition was performing well.

Finally, an alternate derivation for the analytic vacuum response matrix was used. This simpler derivation is shown in Appendix A.2. When calculated at the GRIN nodes and splined to the NIMROD nodes, this improved convergence to give a rate of approximately 2 irrespective of polynomial degree. So while this was an improvement, it still does not show optimal performance.

	rate	poly degree
base case	1.4	4
matrix at gll nodes	1.0	4
RZ mesh	1.0	3
analytic E_{wall} BC	3.3	3
new matrix	2.2	4

Table 2: Algebraic convergence rates for the various numerical scenarios used to diagnose the convergence problems.

These results, both in the large aspect ratio torus and the periodic cylinder, indicate that the primary source of error is in the calculation of the vacuum magnetic field used in the boundary condition on the electric field in the wall. Because using a vacuum response calculation at the GLL nodes (without the need to interpolate) for the periodic cylinder

did not improve performance, we cannot simply fault the spline interpolation method. Indeed, beyond identifying the electric field boundary condition as the location of the issue, a conclusion was not reached regarding the exact source of error. Nonetheless, the convergence scans served a purpose: they led to the identification of at least one coding error, highlighted the need for an improvement on the average interpolation method, and prompted the derivation of a simplified vacuum response matrix for the periodic cylinder. Additionally, while the convergence rates were too slow, there was convergence, and the percentage error at larger resolutions was sufficiently small to expect qualitatively correct results for RWMs far from marginal stability limits.

Chapter 6

Simulating the RWM in NSTX

The general geometry resistive wall boundary condition was utilized to run equilibria from the National Spherical Torus Experiment (NSTX). Spherical tori have a smaller aspect ratio than a standard tokamak, shaped more like a cored apple than a donut. Among other things, the small aspect ratio leads to an increased coupling of poloidal mode numbers in external kink-like modes such as the RWM. The RWM in NSTX is often stabilized by kinetic effects[36, 67], but may become unstable and interact nonlinearly with plasma rotation.

Equilibrium reconstructions from two similar NSTX shots were the basis for this work. In both shots, normalized beta (β_N) was scanned through the $n = 1$ no-wall stability limit. In ideal MHD, with no equilibrium rotation, this no-wall β_N limit corresponds to the RWM stability limit. We take advantage of this by running NIMROD with parameters which approach the ideal plasma-ideal vacuum limit, where a high resistivity, lower density region approximates a vacuum between the plasma separatrix and the resistive wall. These results could then be compared to the no-wall stability of such an idealized equilibrium calculated by stability code DCON, as is presented in Section 6.3.

6.1 Modeling NSTX with NIMROD

The NSTX equilibria studied are EFIT [89] reconstructions from shots 140110 and 140137. The edge of the NIMROD domain is defined by a smooth boundary at locations close to

the innermost NSTX wall locations. On the outboard side, this includes the toroidally segmented symmetric copper stabilizing plates that circle the device - two above and two below the midplane [88]. The NIMROD domain is shown super-imposed on a diagram of the experimental cross-section in Fig. 21.

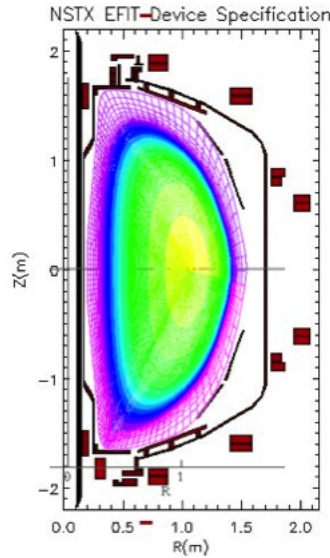


Figure 21: Comparison of real and NIMROD wall locations for NSTX

Because the desired spatial resolution for a NIMROD run is significantly larger than the resolution used for EFIT reconstructions, we made use of a recently developed NIMROD preprocessor, FLUXGRID-NIMEQ. FLUXGRID-NIMEQ solves for a Grad-Shafranov equilibrium with the NIMROD basis functions using the EFIT reconstruction for the pressure and toroidal magnetic field profiles and the magnetic-flux boundary condition, then regrids the domain to be flux-surface-aligned. This process may be iterated to improve the NIMROD equilibrium. Along with the equilibrium profiles supplied by EFIT, the plasma resistivity and viscosity are set such that the plasma evolution is still well-described by ideal MHD. For these runs, resistivity is set so that the Lundquist number $S = 10^8$ and the viscosity is set so that the magnetic Prandtl number $P_m = 1$. Additionally, the equilibrium number density is set to be constant throughout the plasma at $n_0 = 4 \times 10^{19}$. Representative

pressure and safety factor profiles are shown in Figs. 22 and 23 from times in both shots with intermediate β_N .

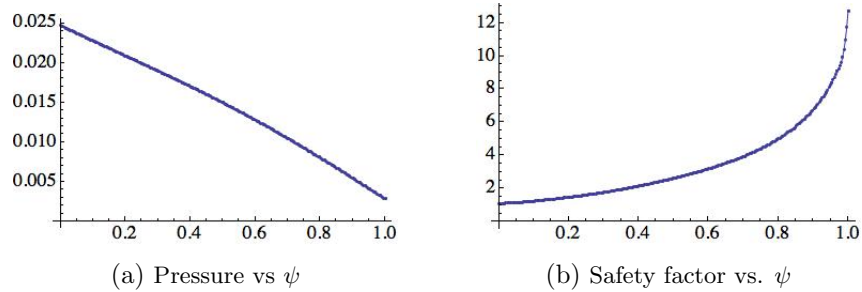


Figure 22: Equilibrium profiles for NSTX shot 140110 at $t = 367ms$ when $\beta_N = 5.55$

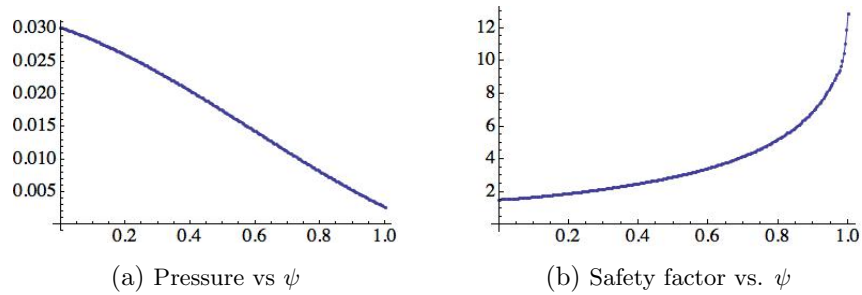


Figure 23: Equilibrium profiles for NSTX shot 140137 at $t = 439ms$ when $\beta_N = 5.47$

While the equilibrium inside the separatrix is primarily determined by the EFIT reconstruction, the equilibrium outside the separatrix must be specified by the user. For an idealized equilibrium, there is a sharp transition from the bulk plasma to the vacuum-like region between the separatrix and the wall. A step-function transition for resistivity, number density, and temperature is imposed by directly setting these equilibrium quantities to their vacuum-like values at quadrature points outside the separatrix. Resistivity in the vacuum region is set to be a factor of 10^7 larger while number density is set to be a factor of 10^3 smaller. The temperature is set to maintain C0 continuity. Because the perturbed fields may also vary rapidly near the plasma-vacuum-interface, the radial grid is packed around the separatrix to fully resolve all perturbed fields.

6.2 Resistive wall parameter scan

A reconstruction from shot 140137 in which $\beta_N = 6.03$, known to be above the $n = 1$ no-wall limit but below the with-wall limit, was chosen to do a simple scan of the resistive wall parameter, v_{wall} . Behavior of the RWM in simpler geometries suggested that as v_{wall} approached 0, so should the RWM growth rate, and that as v_{wall} increased, the growth rate should increase monotonically as well. This was seen in the results of the scan, as shown in Fig. 24. The eigenmode structure observed in the perturbed fields remained the same for different wall parameters. The magnetic field contours in Fig. 25 show a global mode extending past the separatrix to the wall, with large lobes on the outboard side and increasingly small structure on the inboard side, demonstrative of the large amount of poloidal mode coupling caused by the geometry of NSTX. The perturbed pressure profile shown in Fig. 25c has some noise outside the separatrix, but is otherwise limited to within the separatrix, with similarly highly shaped structures.

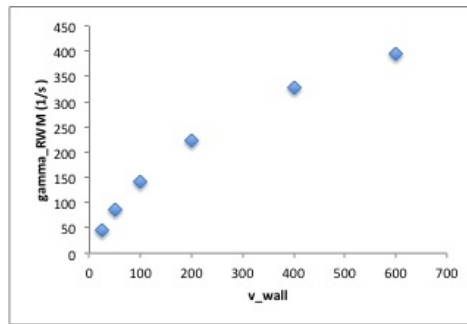


Figure 24: RWM growth rate vs. wall parameter v_{wall} for NSTX shot 140137 at $\beta_N = 6.03$

6.3 Identifying the critical β_N for RWM stability

NSTX shots 140110 and 140137 scan β_N through the $n = 1$ no-wall stability limit. The safety factor on-axis, q_0 , also varies throughout these shots, though not monotonically. To begin, only a sample of the time slices (see Figs. 26 and 27) were examined in order

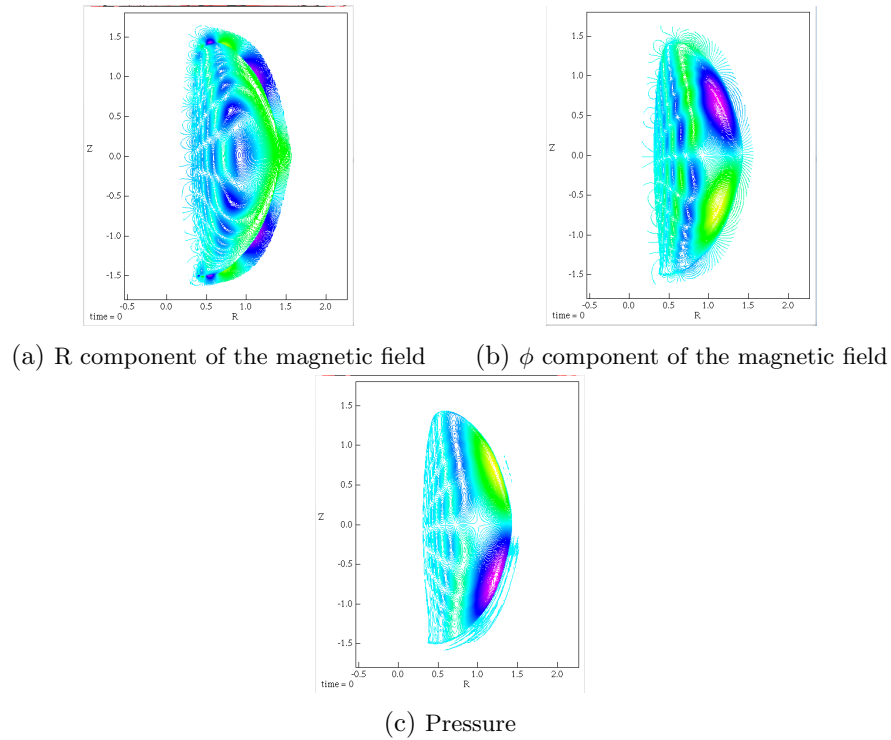


Figure 25: Perturbed field contours at $t = 439ms$ of shot 140137

to determine a possible range for $\beta_{N,crit}$. After preprocessing with FLUXGRID-NIMEQ, the equilibria from these time slices were run using the standard perfectly-conducting wall boundary condition in NIMROD, in order to ensure that the grid and preprocessing were sufficient to prevent a numerical mode (particularly near the x-point) and to demonstrate that the equilibrium was ideal-wall stable.

The $n=1$ RWM growth rates for the sampled values of β_N are shown in Figs. 28 and 29. These are shown with a linear fit for the non-zero growth rate cases, used to calculate an estimated $\beta_{N,crit}$. However, the margin of error in this prediction (from the standard deviation of the fit) is large: as much as 29% of the calculated stability limit for shot 140137, and we conclude that we can only predict the range in which $\beta_{N,crit}$ falls based on this sample of time slices. The results from shot 140137 at $\beta_N = 4.45$ make even the range prediction difficult, as the kinetic and magnetic energies showed small scale

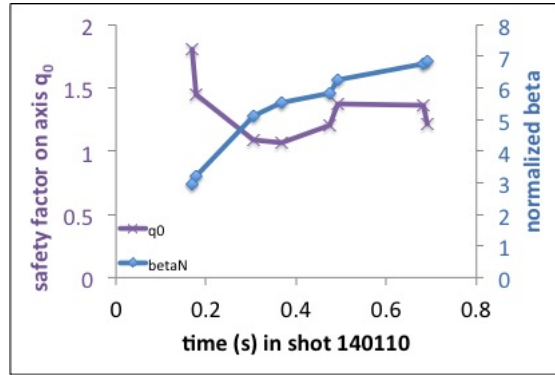


Figure 26: β_N and safety factor for sample of time slices from NSTX shot 140110

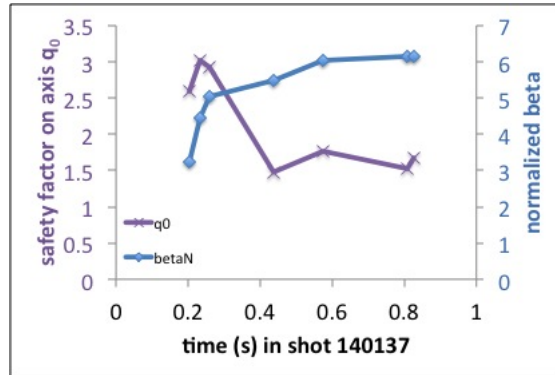


Figure 27: β_N and safety factor for sample of time slices from NSTX shot 140137

oscillations at a low level (similar to those seen in Fig. 31) and the RWM eigenfunction was present in the perturbed magnetic fields. From this it was initially concluded that this equilibrium was at marginal stability. These scans indicated that for shot 140110, $3.2 < \beta_{N,crit} < 5.1$, and for shot 140137, $4.45 \leq \beta_{N,crit} < 5.05$. Preliminary DCON results for these shots were consistent with the NIMROD results, with $\beta_{N,crit} < 4.55$ for shot 140110, and $3.82 < \beta_{N,crit} < 4.63$ for shot 140137. These scans were reproduced using different resistive wall parameters, which led to different growth rate amplitudes, but the same $\beta_{N,crit}$ predicted by the linear fit.

From here, a more precise result was sought for shot 140137, based on a new series of reconstructions at multiple time slices within the predicted range. The reconstructions at

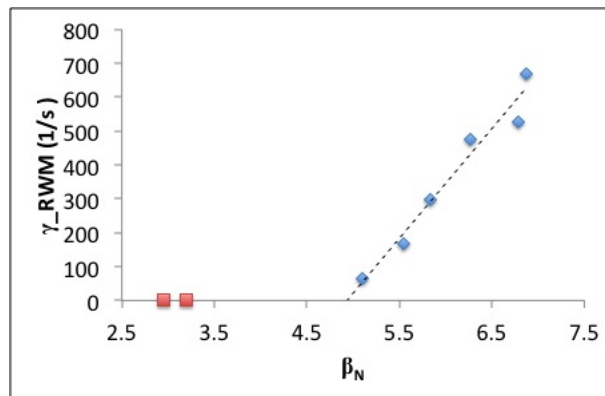


Figure 28: RWM growth rate vs. β_N for shot 140110, with unstable and marginally stable RWMs in blue diamonds and stable β_N s in red squares. A linear best-fit line is shown.

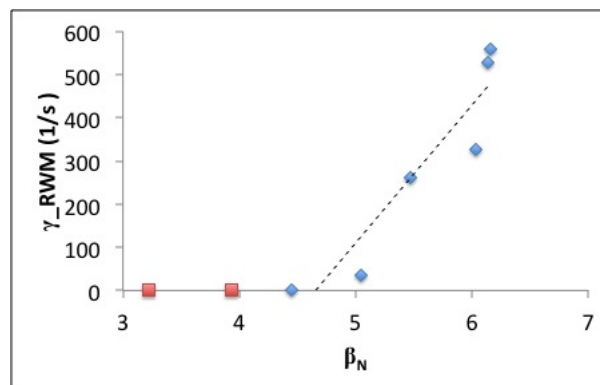


Figure 29: RWM growth rate vs. β_N for shot 140137, with unstable and marginally stable RWMs in blue diamonds and stable β_N s in red squares. A linear best-fit line is shown.

the end points of this range were slightly different, presumably due to small modifications in EFIT parameters, as can be seen in the plot of β_N vs. time in Fig. 30. For the lower bound of this range (previously believed to be marginally stable,) the RWM in NIMROD had a non-zero growth rate. Furthermore, two equilibria with intermediate β_N in this series produced the slowly oscillating energies with no significant growth that was originally hypothesized to indicate marginal stability, shown in Fig. 31. These results were not included in the data plotted in Fig. 32. They may be instances in which, at least for the time scale simulated, the stable rotating solution to the RWM equations is for some reason settled upon. Besides these two cases, no equilibria in this range appear to be stable to

the RWM. This was confirmed by DCON results, which calculated $3.95 < \beta_{N,crit} < 4$.

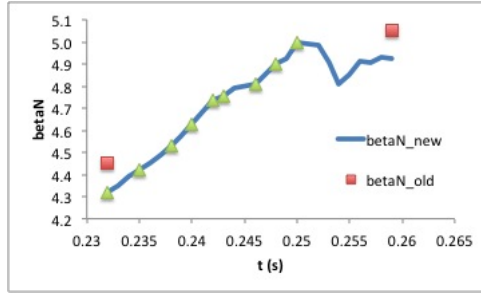


Figure 30: Intermediate range of β_N vs time for shot 140137

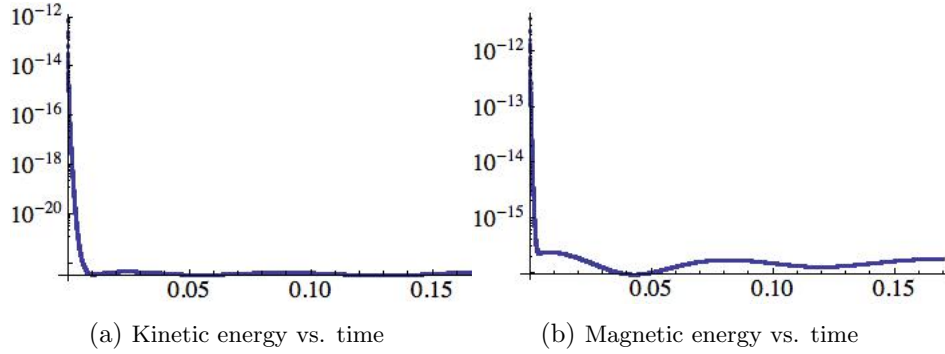


Figure 31: Low level energy oscillations for $t = 0.242s$ of shot 140137

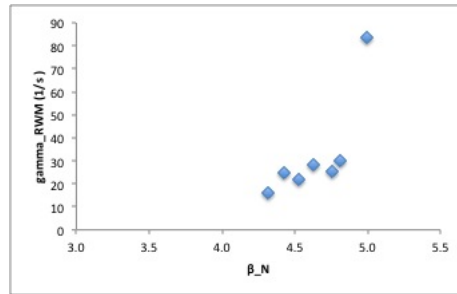


Figure 32: RWM growth rates for intermediate range of β_N

A third series of equilibrium reconstructions with β_N ranging from 3.95 to 4.39 was run in NIMROD. For all but two of the equilibria run in this range, no growing mode appeared. The trend shown by the growth rates of the two cases with RWMs and their β_N relative to the cases with no mode growth was the opposite of what was expected.

The probable cause of this inconsistency is the computational error responsible for the poor convergence discussed in Section 5.3. While small errors such as these may not be physically significant for a highly unstable mode with a large growth rate, they may skew the resistive wall response enough to make an unstable equilibrium appear stable or vice versa. In this way they hinder the capability of NIMROD with this resistive wall boundary condition to predict RWM stability limits. The conclusion of these three series of β_N scans is that NIMROD with the presently implemented resistive wall boundary condition can accurately predict a possible range for $\beta_{N,crit}$ among a set of equilibria that samples β_N sufficiently often to avoid being misled by an equilibrium that takes much longer to find the RWM. However, a precise stability limit cannot be determined because of the error introduced by the boundary condition.

Chapter 7

Conclusions

The resistive wall boundary condition in NIMROD provides a tool to simulate RWMs to better understand their stability and behavior. The process of developing and testing a boundary condition that is applicable even for a highly shaped tokamak included a range of RWM simulations as well as a foray into the study of error fields and mode locking made possible by an extension of the periodic cylinder boundary condition. The analytically simple periodic cylinder equilibrium used as a test case for initial development was useful for testing the accuracy and convergence properties of the more general boundary condition. It also was the basis for the equilibrium used in the circular-cross-section large-aspect-ratio tests of the general boundary condition.

The general boundary condition was able to reproduce the results of the analytic periodic cylinder boundary condition for the standard RWM-unstable equilibrium. The RWM growth rate in the large-aspect-ratio torus approached the analytic periodic cylinder growth rate as the aspect ratio was increased, while the eigenfunction was similar to the periodic cylinder eigenfunction but with slight differences due to poloidal-mode coupling. Convergence studies using the general boundary condition for both the periodic cylinder and the large-aspect-ratio torus did not meet the standards for a spectral element code, with slow h-convergence rates that did not improve with increasing polynomial degree. This poor convergence indicated a source of error in the boundary condition which could make quantitative RWM results, especially near marginal stability, unreliable. However, for very unstable RWMs, this boundary condition still allows for useful simulation results,

with the caveats that there is greater uncertainty in the growth rate and that increasing resolution will have less effect on the accuracy of the result.

The resistive wall boundary condition was used in simulation of the NSTX spherical tokamak. The plasma equilibrium was set using EFIT reconstructions and the region outside the separatrix was a low-density, high-resistivity plasma that represents the vacuum between the plasma and wall. The NSTX shots studied scanned β_N across the RWM stability limit. For a time with large β_N , the RWM in NIMROD was unstable and its structure and linear growth rate were determined. A series of reconstructions from times with different β_N s was used to predict the critical β_N for RWM stability. While the use of NIMROD enabled the identification of a broad range in which the critical stability limit must lie, it could not identify a precise critical value. Near marginal stability, the growth rates did not show a clear trend. This shortcoming was mostly likely due to the error shown by the convergence studies.

Despite this, the resistive wall boundary condition in NIMROD can be a useful tool to better understand RWM physics. In particular, the non-linear simulation of NSTX equilibria with toroidal rotation using the resistive wall boundary condition may provide new insight into the non-linear interaction of the mode, the wall, and the rotating plasma.

Appendix A

Derivation of Vacuum Response Matrix for Periodic Cylinder

A.1 Method 1

We begin with Green's Second Theorem:

$$\int_V (\chi \nabla^2 \psi - \psi \nabla^2 \chi) dV = \oint_S \left(\chi \frac{\partial \psi}{\partial n} - \psi \frac{\partial \chi}{\partial n} \right) dS \quad (\text{A.1})$$

Here, χ is the scalar defining the vacuum magnetic field (where $\nabla^2 \chi = 0$), and we chose ψ to be the Green function G where $\nabla^2 G = -4\pi\delta(\mathbf{x} - \mathbf{x}')$. Now, with all known values on the RHS, and what will become the inverse vacuum response matrix on the LHS multiplying χ , we have:

$$\oint_{S'} [4\pi\delta(\mathbf{x} - \mathbf{x}') + \hat{n} \cdot \nabla' G(\mathbf{x}, \mathbf{x}')] \chi(\mathbf{x}') dS' = \oint_{S'} G(\mathbf{x}, \mathbf{x}') \hat{n} \cdot \nabla' \chi dS' \quad (\text{A.2})$$

$$\hat{n} \cdot \nabla' \chi = B_{norm} \quad (\text{A.3})$$

$$\chi(x) = \sum_{m,k=-\infty}^{\infty} \chi_{m,k}(r) e^{i(m\theta+kz)} \quad (\text{A.4})$$

We can solve for G assuming periodicity in the poloidal and axial directions.

$$\nabla^2 G = \frac{4\pi}{r} \delta(r - r') \delta(\theta - \theta') \delta(z - z') \quad (\text{A.5})$$

$$\delta(\xi - \xi') = \frac{1}{2\pi} \sum_{j=-\infty}^{\infty} e^{ij(\theta - \theta')} \quad (\text{A.6})$$

$$\frac{1}{r} \frac{\partial}{\partial r} \left[r \frac{\partial G}{\partial r} \right] + \frac{1}{r^2} \frac{\partial^2 G}{\partial \theta^2} + \frac{\partial^2 G}{\partial z^2} = -\frac{1}{r\pi} \delta(r - r') \sum_{m,k=-\infty}^{\infty} e^{i[m(\theta - \theta') + k(z - z')]} \quad (\text{A.7})$$

$$G(r, \theta, z, r', \theta', z') = \frac{1}{4\pi^2} \sum_{m,k=-\infty}^{\infty} g_{m,k}(r, r') e^{i[m(\theta - \theta') + k(z - z')]} \quad (\text{A.8})$$

$$\frac{1}{r} \frac{\partial}{\partial r} \left[r \frac{\partial g_{m,k}}{\partial r} \right] - \frac{m^2}{r^2} g_{m,k} - k^2 g_{m,k} = -\frac{4\pi}{r} \delta(r - r') \quad (\text{A.9})$$

This gives modified Bessel function solutions (for $k \neq 0$.) We take a cue from Jackson's Classical Electrodynamics[68] and note that we should solve for constants of our solutions using the Wronskian, which should be proportional to $1/x$ for all values of x , so we can evaluate it using the limiting forms of the modified Bessel functions for small x .

$$g_{m,k} = g_{m,k}^<(kr_<) g_{m,k}^>(kr_>) \quad (\text{A.10})$$

$$g_{m,k}^< = AI_m(kr_<) \quad (\text{A.11})$$

$$g_{m,k}^> = K_m(kr_>) \quad (\text{A.12})$$

$$W[g^<(r), g^>(r)] = -\frac{4\pi}{r} \quad (\text{A.13})$$

$$A = 4\pi \quad (\text{A.14})$$

$$G(r, \theta, z, r', \theta', z') = \frac{1}{\pi} \sum_{m,k=-\infty}^{\infty} I_m(kr_<) K_m(kr_>) e^{i[m(\theta - \theta') + k(z - z')]} \quad (\text{A.15})$$

We can also easily find the solution for $k = 0$. We note that the correct form includes

the absolute value of m , which will be useful when we convert this to a purely real form.

$$g_{m,0} = g_{m,0}^<(r_<)g_{m,0}^>(r_>) \quad (\text{A.16})$$

$$g_{m,0}^< = Ar_<^{|m|} \quad (\text{A.17})$$

$$g_{m,0}^> = r_>^{-|m|} \quad (\text{A.18})$$

$$W [g^<(r), g^>(r)] = -\frac{2}{r} \quad (\text{A.19})$$

$$A = \frac{1}{|m|} \quad (\text{A.20})$$

Now we can use this in Eq.(A.2) (along with the Fourier decomposition of χ .)

$$4\pi \sum_{m,k=-\infty}^{\infty} \chi_{m,k}(r_w) e^{i(m\theta+kz)} \quad (\text{A.21})$$

$$+\frac{1}{\pi} \int_0^{2\pi} r_w d\theta' \int_0^{2\pi} dz' \left[\sum_{m,k=-\infty}^{\infty} \frac{dg_{m,k}(r_w, r')}{dr'} e^{i[m(\theta-\theta')+k(z-z')]} \right] \times \left[\sum_{\ell,n=-\infty}^{\infty} \chi_{\ell,n}(r') e^{i(\ell\theta'+nz')} \right] \quad (\text{A.22})$$

$$= \frac{1}{\pi} \int_0^{2\pi} r_w d\theta' \int_0^{2\pi} dz' \left[\sum_{m,k=-\infty}^{\infty} g_{m,k}(r_w, r') e^{i[m(\theta-\theta')+k(z-z')]} \right] \times \left[\sum_{\ell,n=-\infty}^{\infty} \hat{n} \cdot \mathbf{B}_{\ell,n}(r') e^{i(\ell\theta'+nz')} \right] \quad (\text{A.23})$$

We can do some almost trivial simplifications in first the LHS integral:

$$= \frac{r_w}{\pi} \sum_{m,k=-\infty}^{\infty} \sum_{\ell,n=-\infty}^{\infty} \frac{dg_{m,k}}{dr'} \chi_{\ell,n}(r') e^{i(m\theta+kz)} \int_0^{2\pi} d\theta' e^{i(\ell-m)\theta'} \int_0^{2\pi} dz' e^{i(n-k)z'} \quad (\text{A.24})$$

$$= \frac{r_w}{\pi} \sum_{m,k=-\infty}^{\infty} \sum_{\ell,n=-\infty}^{\infty} \frac{dg_{m,k}}{dr'} \chi_{\ell,n}(r') e^{i(m\theta+kz)} (2\pi)^2 \delta_{\ell m} \delta_{nk} \quad (\text{A.25})$$

$$= 4\pi r_w \sum_{m,k=-\infty}^{\infty} \frac{dg_{m,k}}{dr'} \chi_{m,k}(r') e^{i(m\theta+kz)} \quad (\text{A.26})$$

And then the RHS integral

$$= \frac{r_w}{\pi} \sum_{m,k=-\infty}^{\infty} \sum_{\ell,n=-\infty}^{\infty} g_{m,k} B_{norm,\ell,n}(r') e^{i(m\theta+kz)} \int_0^{2\pi} d\theta' e^{i(\ell-m)\theta'} \int_0^{2\pi} dz' e^{i(n-k)z'} \quad (\text{A.27})$$

$$= 4\pi r_w \sum_{m,k=-\infty}^{\infty} g_{m,k} B_{norm,m,k}(r') e^{i(m\theta+kz)} \quad (\text{A.28})$$

Now, we want to include the discrete inverse Fourier transform to put everything in terms of θ . There is a normalization needed for the Fourier transform: here it is denoted simply as the constant C_F . Note that here, r' is at the wall, and r external to the wall, therefore, $r' = r_<$ and $r = r_>$. We are dropping the k dependence, since we want the k Fourier components of χ and \mathbf{B} .

$$\chi(r_w, \theta) + |k|r_w \sum_{m=-\infty}^{\infty} I'_m(kr') K_m(kr) C_F \sum_{j=0}^{N-1} \chi(r_w, \theta_j) e^{-im\theta_j} e^{im\theta} \quad (\text{A.29})$$

$$= r_w \sum_{m=-\infty}^{\infty} I_m(kr') K_m(kr_w) C_F \sum_{j=0}^{N-1} B_{norm}(r_w, \theta_j) e^{im\theta_j} e^{im\theta} \quad (\text{A.30})$$

We will also note that $I_m = I_{-m}$ and $K_m = K_{-m}$ and we'll be able to see how that allows us to write this as a totally real equation. (Here, dropping the radial dependence of χ and \mathbf{B} , and assuming that that Bessel functions and their derivatives are evaluated at kr_w . Derivatives are with respect to kr .)

$$\chi(\theta_i) + |k|r_w C_F \sum_{j=0}^{N-1} \chi(\theta_j) \left[I'_0 K_0 + 2 \sum_{m=1}^{\infty} I'_m K_m \cos[m(\theta_i - \theta_j)] \right] \quad (\text{A.31})$$

$$= r_w C_f \sum_{j=0}^{N-1} B_{norm}(\theta_j) \left[I_0 K_0 + 2 \sum_{m=1}^{\infty} I_m K_m \cos([m(\theta_i - \theta_j)] \right] \quad (\text{A.32})$$

Here you can see that the units work out, since we define $\mathbf{B} = \nabla\chi$, χ has units of tesla * meters. The matrix multiplying B_{norm} has units meters. Now we'll write this in a rough matrix form.

$$\left(\overleftarrow{\mathbf{I}} + \overleftarrow{\mathbf{P}}\right)_n \chi_n = \overleftarrow{\mathbf{Q}}_n B_{norm}^n \quad (\text{A.33})$$

$$\chi_n = \left(\overleftarrow{\mathbf{I}} + \overleftarrow{\mathbf{P}}\right)_n^{-1} \overleftarrow{\mathbf{Q}}_n B_{norm}^n \quad (\text{A.34})$$

$$\mathbf{P}_{ij}^n = |k| r_w C_F \left[I_0' K_0 + 2 \sum_{m=1}^{\infty} I_m' K_m \cos \left[\frac{2\pi m}{N} (i - j) \right] \right] \quad (\text{A.35})$$

$$\mathbf{Q}_{ij}^n = r_w C_F \left[I_0 K_0 + 2 \sum_{m=1}^{\infty} I_m K_m \cos \left[\frac{2\pi m}{N} (i - j) \right] \right] \quad (\text{A.36})$$

Similarly, we can use Eqs.(A.16-A.20) to find the matrix for $k = 0$.

$$\mathbf{P}_{ij}^0 = C_F \left[1 + 2 \sum_{m=1}^{\infty} \cos \left[\frac{2\pi m}{N} (i - j) \right] \right] \quad (\text{A.37})$$

$$\mathbf{Q}_{ij}^0 = r_w C_F \left[2 \sum_{m=1}^{\infty} \frac{1}{|m|} \cos \left[\frac{2\pi m}{N} (i - j) \right] \right] \quad (\text{A.38})$$

A.2 Method 2

We can start with the calculation of the m, n Fourier component of χ , and then transform it back into a function of location on the wall (in this case, just θ_i). Quantities with a bar (\bar{A}) signify the m, n Fourier component, and those same quantities without a bar signify the n Fourier component in real poloidal space. As before, $k = -n/R$.

$$\bar{\chi} = p_1 K_m(|k|r) e^{i(\omega t + m\theta + kz)} \quad (\text{A.39})$$

We use the continuity of the normal magnetic field as a boundary condition to eliminate the unknown constant.

$$\hat{r} \cdot [\mathbf{B}_v - \mathbf{B}_p] = 0 \quad (\text{A.40})$$

$$\bar{B}_{pn}(r_w) = \bar{B}_{vn}(r_w) \quad (\text{A.41})$$

$$p_1 = \frac{-\bar{B}_{pn}(r_w)}{K'_m(|k|r_w)} \quad (\text{A.42})$$

$$\bar{\chi} = -\bar{B}_{pn}(r_w) \frac{K_m(|k|r_w)}{K'_m(|k|r_w)} e^{i(\omega t + m\theta + kz)} \quad (\text{A.43})$$

We use the following discrete Fourier transform and inverse transform to first write \bar{B}_{pn} in terms of $B_{pn}(\theta)$ and then find $\chi(\theta)$. It should be noted that these transforms have exponents of the opposite sign than the common convention so that the rest of the math agrees with nimrod conventions.

$$\bar{f}_{nm}(r) = \sum_{j=0}^{N-1} f_n(r, \theta_j) e^{im\theta_j} \quad (\text{A.44})$$

$$f_n(r, \theta_j) = \sum_m \frac{\bar{f}_{nm}(r)}{N_{pts}} e^{-im\theta_j} \quad (\text{A.45})$$

$$\bar{\chi} = \frac{-K_m(|k|r_w)}{K'_m(|k|r_w)} \sum_{j=0}^{N-1} B_{pn}(\theta_j) e^{im\theta_j} \quad (\text{A.46})$$

$$\chi(\theta_i) = \sum_m \frac{-K_m(|k|r_w)}{N_{pts} K'_m(|k|r_w)} \sum_{j=0}^{N-1} B_{pn}(\theta_j) e^{-im(\theta_i - \theta_j)} \quad (\text{A.47})$$

Thus, we can define $M(w, w')$, or in this case, $M(\theta_i, \theta_j)$.

$$M(\theta_i, \theta_j) = \sum_m \frac{-K_m(|k|r_w)}{N_{pts} K'_m(|k|r_w)} e^{-im(\theta_i - \theta_j)} \quad (\text{A.48})$$

As in the Green's function method, we can write this as a real-valued matrix.

$$M(\theta_i, \theta_j) = \frac{-K_0(|k|r_w)}{N_{pts} K'_0(|k|r_w)} - 2 \sum_{m=1}^{\infty} \frac{K_m(|k|r_w)}{N_{pts} K'_m(|k|r_w)} \cos[m(\theta_i - \theta_j)] \quad (\text{A.49})$$

Appendix B

General Normal Magnetic Field Boundary Condition

Using a weak form to find the change in the normal component of B:

$$\Delta B_n^n e^{in\phi} = \Delta t \left[-\hat{n} \cdot \nabla \times (\mathbf{E}^n e^{in\phi}) \right] \quad (\text{B.1})$$

$$= -e^{in\phi} \Delta t \hat{n} \cdot [\nabla \times \mathbf{E}^n + in \nabla \phi \times \mathbf{E}^n] \quad (\text{B.2})$$

$$\alpha \Delta B_n^n = -\alpha \Delta t \hat{n} \cdot [\nabla \times \mathbf{E}^n + in \nabla \phi \times \mathbf{E}^n] \quad (\text{B.3})$$

$$\alpha \hat{n} \cdot \nabla \times \mathbf{E}^n = \nabla \cdot (\mathbf{E}^n \times \alpha \hat{n}) + \mathbf{E}^n \times (\alpha \hat{n}) \quad (\text{B.4})$$

$$\int_S \alpha \frac{\Delta B_n^n}{\Delta t} dS = - \int_S \left[\nabla \cdot (\mathbf{E}^n \times \alpha \hat{n}) + \mathbf{E}^n \cdot \nabla \times (\alpha \hat{n}) - \frac{in\alpha}{R} E_\theta^n \right] dS \quad (\text{B.5})$$

We can explicitly define the normal unit vector \hat{n} :

$$\hat{n} = \frac{\nabla V}{|\nabla V|} = \frac{\frac{dZ}{d\tau} \hat{R} - \frac{dR}{d\tau} \hat{Z}}{\left(\left(\frac{dZ}{d\tau} \right)^2 + \left(\frac{dR}{d\tau} \right)^2 \right)^{1/2}} \quad (\text{B.6})$$

The following drops the toroidal mode number n superscript for the electric field.

$$\text{RHS} = - \int_S \left[\nabla \cdot (\mathbf{E} \times \alpha \hat{n}) + \mathbf{E} \cdot \nabla \times \left(\frac{\alpha}{|\nabla V|} \nabla V \right) - \frac{in\alpha}{R} E_\theta \right] dS \quad (\text{B.7})$$

$$= - \int_S \left[\nabla \cdot (\mathbf{E} \times \alpha \hat{n}) + \mathbf{E} \cdot \left(\frac{\alpha}{|\nabla V|} \nabla \times \nabla V + \nabla \left(\frac{\alpha}{|\nabla V|} \right) \times \nabla V \right) - \frac{in\alpha}{R} E_\theta \right] dS \quad (\text{B.8})$$

$$= \int_S \left[-\nabla \cdot (\mathbf{E} \times \alpha \hat{n}) + \mathbf{E} \cdot \left[\hat{n} \times \left(\nabla \alpha - \frac{\alpha}{|\nabla V|} \nabla (|\nabla V|) \right) \right] + \frac{in\alpha}{R} E_\theta \right] dS \quad (\text{B.9})$$

$$= \int_S \left[-\nabla \cdot (\mathbf{E} \times \alpha \hat{n}) + E_\phi \left(\frac{1}{|\nabla V|} \frac{d\alpha}{d\tau} - \frac{\alpha}{|\nabla V|^2} \frac{d(|\nabla V|)}{d\tau} \right) + \frac{in\alpha}{R} E_\theta \right] dS \quad (\text{B.10})$$

The differential element dS is defined as:

$$dS = J|\nabla V|d\tau d\phi \quad (\text{B.11})$$

We express the total derivative in terms of the Jacobian, and realize that there will be no normal derivatives because of the direction of the term being operated on, and no toroidal derivatives because this is entirely accounted for by the Fourier decomposition. Furthermore, the identity used does not assume unit basis vectors, so we must divide by the scale factor ($|\nabla V|$) when calculating the θ component. Now we express the total derivative multiplied by dS as a total derivative multiplied by $d\tau$ plus any other terms (multiplied by dS .)

$$-\nabla \cdot (\mathbf{E} \times \alpha \hat{n}) dS = -\frac{1}{J} \frac{d}{d\tau} ((\mathbf{E} \times \alpha \hat{n})_\theta J) J|\nabla V|d\tau d\phi \quad (\text{B.12})$$

$$= -\frac{d}{d\tau} ((\mathbf{E} \times \alpha \hat{n})_\theta J) |\nabla V|d\tau d\phi \quad (\text{B.13})$$

$$= -\frac{d}{d\tau} ((\mathbf{E} \times \alpha \hat{n})_\theta J|\nabla V|) d\tau d\phi + (\mathbf{E} \times \alpha \hat{n})_\theta J \frac{d}{d\tau} (|\nabla V|) d\tau d\phi \quad (\text{B.14})$$

The first term above is a total τ derivative to be integrated over a closed loop in differential element $d\tau$. Its contribution will be zero.

$$-\nabla \cdot (\mathbf{E} \times \alpha \hat{n}) dS = (\mathbf{E} \times \alpha \hat{n})_\theta \frac{1}{|\nabla V|} \frac{d}{d\tau} (|\nabla V|) dS \quad (\text{B.15})$$

$$= E_\phi \frac{\alpha}{|\nabla V|^2} \frac{d(|\nabla V|)}{d\tau} dS \quad (\text{B.16})$$

Now, substituting this back into Eqn. B.10 gives:

$$RHS = \int_S \left[E_\phi \frac{\alpha}{|\nabla V|^2} \frac{d(|\nabla V|)}{d\tau} + E_\phi \left(\frac{1}{|\nabla V|} \frac{d\alpha}{d\tau} - \frac{\alpha}{|\nabla V|^2} \frac{d(|\nabla V|)}{d\tau} \right) + \frac{i\alpha}{R} E_\theta \right] dS \quad (\text{B.17})$$

$$= \int_S \left[E_\phi \frac{1}{|\nabla V|} \frac{d\alpha}{d\tau} + \frac{i\alpha}{R} E_\theta \right] dS \quad (\text{B.18})$$

Bibliography

- [1] E.J. Strait. Stability of high beta tokamak plasmas. *Physics of Plasmas*, 1(5):1415, May 1994.
- [2] M.S. Chu and M. Okabayashi. Stabilization of the external kink and the resistive wall mode. *Plasma Physics and Controlled Fusion*, 52(12):123001, December 2010.
- [3] J. P. Freidberg. *Ideal magnetohydrodynamics*. Plenum Press, New York, 1987.
- [4] R. Fitzpatrick. Bifurcated states of a rotating tokamak plasma in the presence of a static error-field. *Physics of Plasmas*, 5(9):3325, 1998.
- [5] I. B. Bernstein, E. A. Frieman, M. D. Kruskal, and R. M. Kulsrud. An Energy Principle for Hydromagnetic Stability Problems. *Proceedings of the Royal Society A: Mathematical, Physical and Engineering Sciences*, 244(1236):17–40, February 1958.
- [6] F. Troyon, R. Gruber, H Saurenmann, S Semenzato, and S Succi. MHD-Limits to Plasma Confinement. *Plasma Physics and Controlled Fusion*, 26(1A):209–215, January 1984.
- [7] D. Pfirsch and H. Tasso. A theorem on MHD-instability of plasmas with resistive walls. *Nuclear Fusion*, 11(3):259–260, May 1971.
- [8] O Gruber, K Lackner, G. Pautasso, U. Seidel, and B. Streibl. Vertical displacement events and halo currents. *Plasma Physics and Controlled Fusion*, 35(B):191, 1993.
- [9] H.R. Strauss, Linjin Zheng, M. T. Kotschenreuther, W. Park, S.C Jardin, J. Breslau, A. Pletzer, R. Paccagnella, L. Sugiyama, M.S. Chu, M.S. Chance, and A.D Turnbull.

- Halo Current and Resistive Wall Simulations of ITER. In *20th IAEA Fusion Energy Conference*, pages 1–7, 2004.
- [10] R. Paccagnella, M. Cavinato, T. Bolzonella, S. Ortolani, G. Pautasso, W. Schneider, V. Lukash, R. Khayrutdinov, and H.R. Strauss. Vertical displacement events simulations for tokamak plasmas. *Fusion Engineering and Design*, 75-79:589–593, November 2005.
- [11] RD Stambaugh. No Title. In *Plasma Physics and Controlled Fusion Research Conf. (London, UK, 1984)*, page 217, 1985.
- [12] M. Okabayashi. No Title. In *Plasma Physics and Controlled Fusion Research Conf. (Kyoto, Japan, 1986)*, page 275, 1987.
- [13] M. Okabayashi, E.D Fredrickson, J. Manickam, G. Taylor, S.H Batha, M.G Bell, R.V Budny, B.P. LeBlanc, F.M Levinton, J Jackson, K.M McGuire, R. Nazikian, and M.C Zarnstorff. Mode structure of disruption precursors in TFTR enhanced reversed shear discharges. *Nuclear Fusion*, 38(8):1149–1160, August 1998.
- [14] A. Bondeson and D J Ward. Stabilization of external modes in tokamaks by resistive walls and plasma rotation. *Physical review letters*, 72(17):2709, 1994.
- [15] R. Betti and J. P. Freidberg. Stability Analysis of Resistve Wall Kink Modes in Rotating Plasmas. *Physical review letters*, 74(15):2949, 1995.
- [16] R. Fitzpatrick and AY Aydemir. Stabilization of the resistive shell mode in tokamaks. *Nuclear fusion*, 36(1):11, 1996.
- [17] E.J. Strait, T. S. Taylor, A.D Turnbull, J. R. Ferron, L.L. Lao, B. Rice, O. Sauter, S. J. Thompson, and D. Wroblewski. Wall Stabilization of high beta tokamak discharges in DIII-D. *Physical Review Letters*, 74(13):2483, 1995.

- [18] S Takeji, S Tokuda, T. Fujita, T. Suzuki, A. Isayama, S Ide, Y Ishii, Y. Kamada, Y. Koide, T Matsumoto, T Oikawa, T. Ozeki, and Y. Sakamoto. Resistive instabilities in reversed shear discharges and wall stabilization on JT-60U. *Nuclear Fusion*, 42(1):5–13, January 2002.
- [19] E.J. Strait, A.M Garofalo, G.L Jackson, M. Okabayashi, H. Reimerdes, M.S. Chu, R. Fitzpatrick, R. J. Groebner, Y. In, R.J. La Haye, M.J. Lanctot, Y.Q. Liu, G.A Navratil, W.M. Solomon, and H. Takahashi. Resistive wall mode stabilization by slow plasma rotation in DIII-D tokamak discharges with balanced neutral beam injection. *Physics of Plasmas*, 14(5):056101, March 2007.
- [20] M. Takechi, G. Matsunaga, Nobuyuki Aiba, T. Fujita, T. Ozeki, Y. Koide, Y. Sakamoto, G. Kurita, A. Isayama, and Y. Kamada. Identification of a Low Plasma-Rotation Threshold for Stabilization of the Resistive-Wall Mode. *Physical Review Letters*, 98(5):055002, February 2007.
- [21] T.H Jensen, A.W. Leonard, and A.W Hyatt. A simple model for driven islands in tokamaks. *Physics of Fluids B: Plasma Physics*, 5(4):1239, April 1993.
- [22] R. Fitzpatrick. A simple model of the resistive wall mode in tokamaks. *Physics of Plasmas*, 9(8):3459, 2002.
- [23] A.M Garofalo, G.L Jackson, R.J. La Haye, M. Okabayashi, H. Reimerdes, E.J. Strait, J. R. Ferron, R. J. Groebner, Y. In, M.J. Lanctot, G. Matsunaga, G.A Navratil, W.M. Solomon, H. Takahashi, M. Takechi, and A.D Turnbull. Stability and control of resistive wall modes in high beta, low rotation DIII-D plasmas. *Nuclear Fusion*, 47(9):1121–1130, September 2007.
- [24] E.J. Strait, J.M. Bialek, I.N. Bogatu, M.S. Chance, M.S. Chu, D.H Edgell, A.M Garofalo, G.L Jackson, R.J Jayakumar, T.H Jensen, O.N. Katsuro-Hopkins, J.S Kim, R.J.

- La Haye, L.L. Lao, M. A. Makowski, G.A Navratil, M. Okabayashi, H. Reimerdes, J.T Scoville, and A.D Turnbull. Resistive wall mode stabilization with internal feedback coils in DIII-D. *Physics of Plasmas*, 11(5):2505, April 2004.
- [25] A.M Garofalo, M.S. Chu, E.D Fredrickson, M. P. Gryaznevich, T.H Jensen, L.C Johnson, R.J. La Haye, G.A Navratil, M. Okabayashi, J.T Scoville, E.J. Strait, A.D Turnbull, and the DIII-D Team. Resistive wall mode dynamics and active feedback control in DIII-D. *Nuclear Fusion*, 41(9):1171–1176, September 2001.
- [26] T.E. Evans, M.E. Fenstermacher, R.A. Moyer, T.H. Osborne, J.G. Watkins, P. Gohil, I. Joseph, M.J Schaffer, L.R. Baylor, M. Bécoulet, J.A. Boedo, K.H. Burrell, J. S. DeGrassie, K.H. Finken, T. Jernigan, M.W. Jakubowski, C.J Lasnier, M. Lehnen, A.W. Leonard, J. Lonroth, E. Nardon, V. Parail, O. Schmitz, B. Unterberg, and W.P. West. RMP ELM suppression in DIII-D plasmas with ITER similar shapes and collisionalities. *Nuclear Fusion*, 48(2):024002, February 2008.
- [27] R. Fitzpatrick. Stability of coupled tearing and twisting modes in tokamaks. *Physics of Plasmas*, 1(10):3308, October 1994.
- [28] P. H. Rutherford. Nonlinear growth of the tearing mode. *Physics of Fluids*, 16(11):1903, July 1973.
- [29] FL Waelbroeck. Current sheets and nonlinear growth of the $m=1$ kink-tearing mode. *Physics of Fluids B: Plasma Physics*, 1(12):2372, 1989.
- [30] FL Waelbroeck. Onset of the Sawtooth Crash. *Physical review letters*, 70(21):3259–3262, 1993.
- [31] M. Okabayashi, N Pomphrey, and RE Hatcher. Circuit equation formulation of resistive wall mode feedback stabilization schemes. *Nuclear fusion*, 38(11):1607, 1998.

- [32] A.H. Boozer. Error Field Amplification and Rotation Damping in Tokamak Plasmas. *Physical Review Letters*, 86(22):5059–5061, May 2001.
- [33] Ronald S. Irving. *Integers, polynomials, and rings*. Springer-Verlag, New York, 2004.
- [34] A.M Garofalo, T.H Jensen, L.C Johnson, R.J. La Haye, G.A Navratil, M. Okabayashi, J.T Scoville, E.J. Strait, D. R. Baker, J.M. Bialek, M.S. Chu, J. R. Ferron, J. Jayakumar, L.L. Lao, M. a. Makowski, H. Reimerdes, T. S. Taylor, A.D Turnbull, M.R. Wade, and S.K Wong. Sustained rotational stabilization of DIII-D plasmas above the no-wall beta limit. *Physics of Plasmas*, 9(5):1997, May 2002.
- [35] T.C Hender and JET EFDA Contributors. No Title. In *Proc. 20th IAEA Fusion Energy Conf. (Vilamoura, Portugal)*, pages EX/P2–22, 2004.
- [36] S.A. Sabbagh, R.E. Bell, J.E. Menard, D.A Gates, A.C Sontag, J.M. Bialek, B.P. LeBlanc, F.M Levinton, K.L Tritz, and H. Yuh. Active Stabilization of the Resistive-Wall Mode in High-Beta, Low-Rotation Plasmas. *Physical Review Letters*, 97(4):045004, July 2006.
- [37] D.A Gates and T.C Hender. Resistive wall induced forbidden bands of mode rotation frequency on the COMPASS-D tokamak. *Nuclear Fusion*, 36(3):273–282, March 1996.
- [38] C. Paz-Soldan, M. I. Brookhart, C.C Hegna, and C. B. Forest. Wall-locking of kink modes in a line-tied screw pinch with a rotating wall. *Physics of Plasmas*, 19(5):056104, March 2012.
- [39] R. Gruber, F. Troyon, D. Berger, L.C. Bernard, S. Rousset, R. Schreiber, W. Kerner, W. Schneider, and K.V. Roberts. Erato stability code. *Computer Physics Communications*, 21(3):323–371, January 1981.

- [40] R.C Grimm, R. L. Dewar, and J. Manickam. Ideal MHD stability calculations in axisymmetric toroidal coordinate systems. *Journal of Computational Physics*, 49(1):94–117, January 1983.
- [41] L.C. Bernard, F.J. Helton, and R.W. Moore. GATO: An MHD stability code for axisymmetric plasmas with internal separatrices. *Computer Physics Communications*, 24(3-4):377–380, December 1981.
- [42] A. H. Glasser and M.S. Chance. Determination of Free Boundary Ideal MHD Stability with DCON and VACUUM. *Bull. Am. Phys. Soc.*, 42:1848, 1997.
- [43] A. Bondeson, G. Vlad, and H. LuÛltjens. Resistive toroidal stability of internal kink modes in circular and shaped tokamaks. *Physics of Fluids B: Plasma Physics*, 4(7):1889, July 1992.
- [44] Y.Q. Liu, A. Bondeson, C M Fransson, B. Lennartson, and C. Breitholtz. Feedback stabilization of nonaxisymmetric resistive wall modes in tokamaks. I. Electromagnetic model. *Physics of Plasmas*, 7(9):3681, September 2000.
- [45] Yueqiang Liu, M.S. Chu, I T Chapman, and T.C Hender. Toroidal self-consistent modeling of drift kinetic effects on the resistive wall mode. *Physics of Plasmas*, 15(11):112503, November 2008.
- [46] B. Hu and R. Betti. Resistive Wall Mode in Collisionless Quasistationary Plasmas. *Physical Review Letters*, 93(10):105002, September 2004.
- [47] R. Albanese, Y.Q. Liu, A. Portone, G. Rubinacci, and F. Villone. Coupling Between a 3-D Integral Eddy Current Formulation and a Linearized MHD Model for the Analysis of Resistive Wall Modes. *IEEE Transactions on Magnetics*, 44(6):1654–1657, June 2008.

- [48] R. Albanese and G. Rubinacci. Finite element methods for the solution of 3D eddy current problems. *Advances in Imaging and Electron Physics*, 102:1–86, 1997.
- [49] F. Villone, Y. Liu, G. Rubinacci, and S. Ventre. Effects of thick blanket modules on the resistive wall modes stability in ITER. *Nuclear Fusion*, 50(12):125011, 2010.
- [50] J.M. Bialek, A.H. Boozer, M.E. Mauel, and G.A. Navratil. Modeling of active control of external magnetohydrodynamic instabilities. *Physics of Plasmas*, 8(5):2170, May 2001.
- [51] W. Park, E.V. Belova, G.Y. Fu, and X.Z. Tang. Plasma simulation studies using multilevel physics models. *Physics of Plasmas*, 6(5):1796, 1999.
- [52] A. Pletzer. <http://w3.pppl.gov/rib/repositories/NTCC/catalog/Asset/grin.html>.
- [53] N.M. Ferraro, S.C. Jardin, and P. B. Snyder. Ideal and resistive edge stability calculations with M3D-C[sup 1]. *Physics of Plasmas*, 17(10):102508, October 2010.
- [54] N.M. Ferraro, S.C. Jardin, and D. Pfefferle. Modeling resistive wall modes and disruptive instabilities with M3D-C1. In *APS Meeting Abstracts*, October 2016.
- [55] L.-J. Zheng and M. T. Kotschenreuther. AEGIS: An adaptive ideal-magnetohydrodynamics shooting code for axisymmetric plasma stability. *Journal of Computational Physics*, 211(2):748–766, January 2006.
- [56] L.-J. Zheng and M. T. Kotschenreuther. Wall thickness effect on the resistive wall mode stability in toroidal plasmas. *Physics of Plasmas*, 12(7):072504, June 2005.
- [57] L. J. Zheng, M. T. Kotschenreuther, and J.W. Van Dam. Paper TH/P9-32. In *Proc. 22nd IAEA Fusion Energy Conf. (Geneva, Switzerland)*, 2008.
- [58] Olivier Czarny and G.T.A. Huysmans. Bézier surfaces and finite elements for MHD simulations. *Journal of Computational Physics*, 227(16):7423–7445, August 2008.

- [59] M Hölzl, P. Merkel, G.T.A Huysmans, E. Nardon, E. Strumberger, R McAdams, I T Chapman, S Günter, and K Lacker. Coupling JOREK and STARWALL Codes for Non-linear Resistive-wall Simulations. *Journal of Physics: Conference Series*, 401:012010, 2012.
- [60] J.-K. Park, M.J Schaffer, J.E. Menard, and A.H. Boozer. Control of Asymmetric Magnetic Perturbations in Tokamaks. *Physical Review Letters*, 99(19):195003, November 2007.
- [61] C.R. Sovinec, A. H. Glasser, T A Gianakon, D.C. Barnes, R.a. Nebel, S.E. Kruger, D. D. Schnack, S.J. Plimpton, A. Tarditi, and M.S. Chu. Nonlinear magnetohydrodynamics simulation using high-order finite elements. *Journal of Computational Physics*, 195(1):355–386, March 2004.
- [62] R.L. Miller and J.W. Van Dam. Hot particle stabilization of ballooning modes in tokamaks. *Nuclear Fusion*, 27(12):2101–2112, December 1987.
- [63] J. M. Finn. Resistive wall stabilization of kink and tearing modes. *Physics of Plasmas*, 2(1):198, January 1995.
- [64] H.R. Strauss. Nonlinear, three-dimensional magnetohydrodynamics of noncircular tokamaks. *Physics of Fluids*, 19(1):134, 1976.
- [65] HP Furth, P. H. Rutherford, and H Selberg. Tearing mode in the cylindrical tokamak. *Physics of Fluids*, 16(7):1054, July 1973.
- [66] G. Strang and G.J. Fix. *An Analysis of the Finite Element Method*. Prentice-Hall, 1973.
- [67] J.W. Berkery, S.A. Sabbagh, H. Reimerdes, R. Betti, B. Hu, R.E. Bell, S.P. Gerhardt, J. Manickam, and M. Podesta. The role of kinetic effects, including plasma

rotation and energetic particles, in resistive wall mode stability. *Physics of Plasmas*, 17(8):082504, August 2010.

- [68] John David Jackson. 3.11 Expansion of Green Functions in Cylindrical Coordinates. In *Classical Electrodynamics*, pages 125–127. John Wiley & Sons, Inc., New York, third edition, 1999.